8-2011

Development of Reduced Complexity Models for Electromagnetic Modeling

Changyi Su
Clemson University, schangyi@hotmail.com

DEVELOPMENT OF REDUCED COMPLEXITY MODELS FOR ELECTROMAGNETIC MODELING

A Dissertation
Presented to
the Graduate School of
Clemson University

In Partial Fulfillment
of the Requirements for the Degree
Doctor of Philosophy
Electrical and Computer Engineering

---

by
Changyi Su
August 2011

Accepted by:
Todd Hubing, Committee Chair
L. Wilson Pearson
Xiao-Bang Xu
Pierluigi Pisu

ABSTRACT

The current and field distributions of various structures can be calculated using full-wave numerical modeling codes. However, this approach is limited by the complex models and extensive computational resources required to analyze the details of each structure. In addition, brute-force modeling of the entire geometry provides relatively little physical insight into the electromagnetic interference (EMI) source mechanisms. Alternatively an effective equivalent model can be obtained by eliminating sources and structures that do not contribute significantly to the radiated emissions and focusing on the features that could possibly be significant sources of EMI. Equivalent models are generally much simpler than model-everything full-wave models and provide physical insight into the features that have the greatest impact on radiated emissions.

This dissertation includes four chapters on development of reduced complexity models for the modeling of antennas and printed circuit board (PCB) structures. In the first chapter, a simplified model for normal mode helical antennas is proposed. In this model, the highly curved structure of the helix is replaced with straight wires and lumped elements. The simplified model can be used to reduce the complexity of full-wave models that include a helical antenna. It also can be used to estimate the performance of a helical antenna without full-wave modeling of the helical structure.

The second chapter describes a model for determining the common-mode currents on cables attached to a PCB that is based on the concept of imbalance difference. The imbalance difference model is derived from research that shows that changes in

geometrical imbalance cause differential- to common-mode conversion. The imbalance difference model can be used to estimate the radiated emissions from trace-board structures due to common-mode currents induced on attached cables.

The third chapter introduces a new closed-form expression for estimating the maximum radiated emissions from the board-source-cable structure. This expression is based on two improvements to a closed-form expression in a 2008 paper published in the *IEEE Transactions on EMC*. The accuracy of the estimate for larger frequency ranges is improved by using an expression for the envelope of $F(\theta, k, l_{ant})$ that equals the maximum value at every resonant frequency. A modified expression for calculating the effective length of the board improves the accuracy of the estimate when applied to nearly square boards.

In the forth chapter, a modeling technique is proposed to speed up the analysis of PCBs with coupled microstrip lines that induce common-mode currents on attached cables. Based on the concept of imbalance difference, differential-mode sources are converted to equivalent common-mode sources that drive the attached cable and the PCB reference plane. A closed-form expression is also developed based on the imbalance difference model to estimate the maximum radiated emissions from the PCB.

DEDICATION

I dedicate this Doctoral dissertation to my family. I am most especially grateful to my mother, Yunqiu Dang, and father, Yanmin Su, for their continuous love and support. I must also thank my husband, Xinbo He, who has given me extraordinary support and encouragement in the pursuit of academic excellence.

ACKNOWLEDGMENTS

I would like to thank all of these people who helped me make this dissertation possible.

First, I wish to thank my advisor, Dr. Todd Hubing, for all his guidance, support and patience throughout my pursuit of Ph. D. degree. I would also like to thank my Ph. D. degree committee members, Dr. L. Wilson Pearson, Dr. Xiao-Bang Xu, and Dr. Pierluigi Pisu, for their very helpful insights, suggestions, and comments.

I would like to acknowledge all my fellow graduate students in both the Applied Electromagnetics Group and the CVEL laboratory. I appreciate all their technical support and assistance with my research work.

Finally, I would like to thank my understanding and patient husband, Xinbo He, for his encouragement and emotional support.

TABLE OF CONTENTS

Page

LIST OF TABLES

LIST OF FIGURES

CHAPTER ONE

A SIMPLIFIED MODEL FOR NORMAL MODE HELICAL ANTENNAS

Changyi Su, Haixin Ke, and Todd Hubing

ABSTRACT

Normal mode helical antennas are widely used for RFID and mobile communications applications due to their relatively small size and omni-directional radiation pattern. However, their highly curved geometry can make the design and analysis of helical antennas that are part of larger complex structures quite difficult. A simplified model is proposed that replaces the curved helix with straight wires and lumped elements. The simplified model can be used to reduce the complexity of full-wave models that include a helical antenna. It also can be used to estimate the performance of a helical antenna without full-wave modeling of the helical structure.

1.1 INTRODUCTION

The helical antenna was introduced by John D. Kraus in 1946. Based on the far-field radiation pattern, a helical antenna operates in one of two principle modes: the normal mode with the maximum radiation perpendicular to the helix axis; or the axial mode with the maximum radiation in the direction of the axis [1]. The normal mode dominates when the diameter and axial length of the helix are much smaller than a wavelength. The radiation pattern of the normal mode helical antenna is omni-directional and generally similar to the pattern of a short dipole antenna. The self-resonant structure

enables normal mode helical antennas to have radiation characteristics comparable to longer, straight-wire resonant dipole antennas [2]. Hence, normal mode helical antennas find many applications where the physical dimensions of the antennas are important, such as handsets [3], cellular phones [4]-[6] and RFID tags [7].

Unlike straight-wire dipole antennas, helical antennas are three-dimensional in structure and there is a lack of reliable formulas for their design [8]. Most practical designs are the result of physical measurement trial-and-error, which is time-consuming and subject to errors introduced by the measurement facilities [4]. Therefore, numerical techniques are essential to helical antenna design and analysis [9], [10]. Helical antennas are mainly composed of curved surfaces and modeling these antennas using general purpose numerical tools requires mesh elements to be generated to fit the helical wire surfaces. This requires a large density of mesh elements and a great deal of computational resources. When modeling large systems that include a helical antenna, a significant portion of the computational effort may be devoted solely to the analysis of the helix, even when the helix is a small part of the total structure's volume.

In this paper, a simplified model is proposed to speed up the analysis of large structures containing helical antennas. In the simplified model, the helix is approximated by short straight wire segments connected by lumped elements representing the inductance of the helical turns. Theoretical calculations of the equivalent parameters are discussed. Nine different helix configurations are simulated using a general purpose full-wave modeling code to confirm the validity of the proposed model. The resonant frequency and input impedance of each configuration are examined. To further test the

simplified model, two practical examples, an RFID antenna and a handset antenna, are also examined.

1.2 SIMPLIFIED MODEL

Figure 1.1(a) shows the geometry of a helical dipole antenna. The helix is uniformly wound with a constant pitch, *S*. The radius of a helix can be uniform or tapered. In this paper, only uniform helices with constant radius, *R*, are considered. The helix's conductor is a wire of radius, *a*, with a circular cross section. The antenna is fed at the midpoint of the coil winding. In this section, a simplified model of the helix is analyzed and analytical expressions for estimating the model parameters are established.

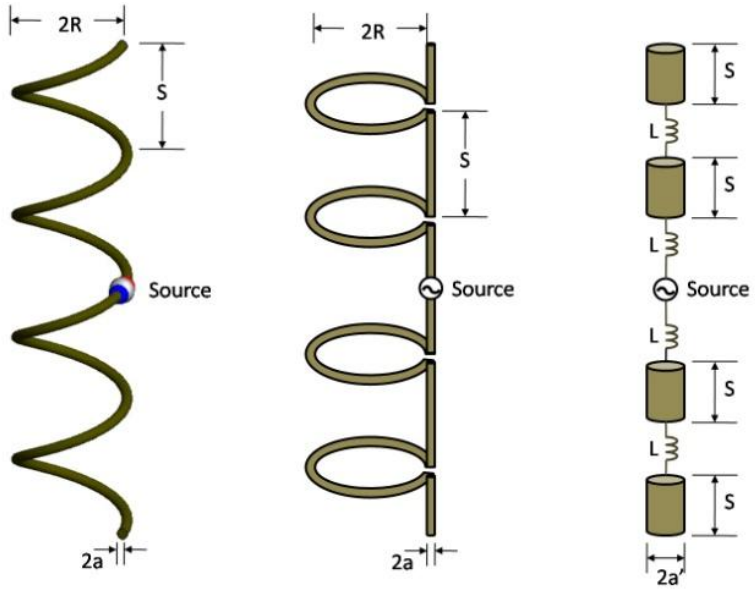

Figure 1.1. (a) Helical antenna. (b) Wire-and-loop model. (c) Wire-and-inductor model.

It has been shown [1] that the helix can be approximated as a series of small loops and dipoles when the physical dimensions of the helix are much smaller than a wavelength. The equivalent wire-and-loop model for the helical antenna is shown in Figure 1.1(b). The wire-and-loop model suggests that the axial ratio of the normal mode helical antenna can be expressed as

$$AR = \frac{E_\theta}{E_\phi} = \frac{2S\lambda}{(2\pi R)^2} = \frac{2S_\lambda}{C_\lambda^2} \tag{1}$$

where $S_\lambda = S/\lambda$ and $C_\lambda = C/\lambda$. C is the circumference of the loop.

Most practical normal-mode helical antennas have an axial ratio greater than 1. In these antennas, the radiated field from the loops is smaller than the radiated field from the straight wire segments. We can generally neglect the radiation from the loops without incurring significant error. For example, if we require 2 dB of accuracy, we can still neglect the field radiated by the loops as long as,

$$\frac{E_\phi + E_\theta}{E_\theta} < 2\,dB \tag{2}$$

Equations (1) and (2) imply that we can neglect the radiation from the loops as long as,

$$AR > 4 \tag{3}$$

From (1), it is clear that different axial ratios can be achieved by proper selection of the helix dimensions. For example, with $C_\lambda < 0.1$, $AR > 4$ is satisfied when $S_\lambda > 0.02$. The limits of the diameter and the pitch of the helix can be better expressed using the definition of pitch angle, e.g. in this case,

$$\tan(\alpha) = \frac{S}{C} > 0.2 \ or \ \alpha > 11^{\circ} \tag{4}$$

When the radiation from the loops can be neglected, they function like inductors. With this in mind, the wire-and-loop model can be further simplified by substituting inductors for the small loops as shown in Figure 1.1(c). The proposed, simplified model consists of one straight wire segment per turn. Each segment is oriented vertically and has a length equal to the pitch of the helix. The segments are connected by lumped, inductive elements. The lumped elements do not increase the size of the mesh and do not significantly add to the computational complexity of the numerical analysis. Therefore, the simplified model requires considerably less computational resources to analyze than the original full-structure analysis.

In the original helix structure, the adjacent turns are coupled together via both mutual inductance and mutual capacitance. Since all the turns are coaxially oriented, some of the magnetic flux generated by one turn will pass through the neighboring turns. This part of flux induces a voltage that has the same polarity as the voltage drop caused by the self-inductance. In addition to the magnetic field coupling, electric field coupling also occurs between turns. The turn-to-turn capacitance provides an alternative current path that bypasses the loop and the straight wire. In the following sections, analytical expressions are derived that compensate for the mutual coupling that is missing in the simplified model.

1.2.1 Equivalent Loop Inductance

The parameters that need to be determined for the wire-and-inductor model in Figure 1(c) include the equivalent inductance *L* of a single turn, and the equivalent radius *a'* of a short wire segment. The equivalent inductance includes the self-inductance L_{self} of one turn and the mutual inductance *M* coupled from its adjacent turns,

$$L = L_{self} + 2M \tag{5}$$

The self inductance of a loop placed in free space is given by the double integral Neumann formula [13],

$$L_{self} = \frac{\mu_0}{4\pi} \oint_C \oint_{C'} \frac{d\vec{l} \bullet d\vec{l}'}{r} \tag{6}$$

where μ_0 is the permeability of free space; and $d\vec{l}$ and $d\vec{l}'$ represent the differential elements on the same wire loop, *C* or *C'*, separated by a distance, *r*. For a circular loop of wire, a closed form approximation for Equation (6) is given by the following expression [13]:

$$L_{loop} = \mu_0 R \left[ln\left(\frac{8R}{a}\right) - 2 \right] \tag{7}$$

where *R* is the loop radius and *a* is the wire radius.

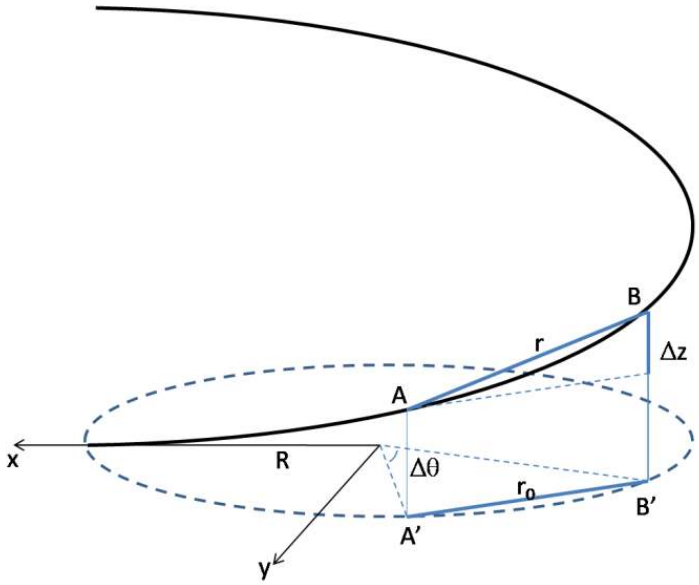

Figure 1.2. Helical curve.

As shown in Figure 1.2, the actual distance between any two points, *A* and *B*, on the helical curve is,

$$r = \sqrt{r_0^2 + \Delta z^2} \tag{8}$$

where r_0 is the distance between *A'* and *B'* obtained by projecting point *A* and *B* onto the x-y plane. Δz is the distance between points *A* and *B* in the *z* direction. When the pitch is small compared to the coil radius, the distance between *A* and *B* is approximately equal to that between *A'* and *B'* or $r \approx r_0$. Therefore, for a small pitch angle, Equation (7) is a good approximation of the self inductance of a helix turn. However, as the pitch angle increases, Δz increases quickly. Consequently, the self inductance of a helix turn with a large pitch angle is much smaller than the inductance calculated by (7). Notice that for any point on the helix curve,

$$\frac{z}{R\theta} = \frac{S}{2\pi R} \tag{9}$$

Therefore,

$$\Delta z = \frac{S}{2\pi R} R\Delta\theta \tag{10}$$

Using the approximation,

$$r_0 \approx R\Delta\theta \tag{11}$$

Equation (8) becomes

$$r = r_0\sqrt{\left(\frac{\Delta z}{r_0}\right)^2 + 1} \approx r_0\sqrt{\left(\frac{S}{2\pi R}\right)^2 + 1} \tag{12}$$

Substituting (12) into (6), the self inductance of a helix turn is given by,

$$\begin{aligned} L_{self} &= \frac{\mu_0}{4\pi}\oint\oint \frac{d\vec{l}\bullet d\vec{l}'}{r} \\ &\approx \frac{\mu_0}{4\pi}\oint\oint \frac{d\vec{l}\bullet d\vec{l}'}{r_0}\frac{1}{\sqrt{\left(\frac{S}{2\pi R}\right)^2 + 1}} \\ &= L_{loop}\frac{2\pi R}{\sqrt{(2\pi R)^2 + S^2}} \\ &= L_{loop}\cos(\alpha) \end{aligned} \tag{13}$$

The mutual inductance between two adjacent turns can be approximated by the mutual inductance between two coaxially oriented circular loops of radius *R*, separated by a distance *S* [13].

$$M = \frac{\pi \mu_0 R^4}{2\left(R^2 + S^2\right)^{\frac{3}{2}}} \tag{14}$$

1.2.2 Equivalent Wire Radius

The capacitance of a wire with length *l* and radius *a* placed in free space is given by [14],

$$C_w = \frac{\pi \varepsilon_0 l}{2ln\left(\frac{l}{a}\right)} \tag{15}$$

where ε_0 is the permittivity of free space. In Figure 1(c), one helix turn is replaced by a short wire segment with a length equal to the helix pitch. The wire length is much shorter than the turn length; therefore, the total wire capacitance is reduced. To maintain the correct capacitance, the radius of the straight wire segments must be increased. The capacitance of the thicker wire should equal the capacitance of a helix turn. Therefore, the equivalent radius, *a'*, is obtained using the following expression:

$$\frac{S}{\ln\left(\frac{S}{a'}\right)} = \frac{l_{tot}}{\ln\left(\frac{l_{tot}}{a}\right)} \tag{16}$$

where $l_{tot} = \sqrt{\left(2\pi R\right)^2 + S^2}$.

The term on the left-hand side of (16) is the capacitance of a wire segment in the simplified model. The term on the right-hand side of (16) is the capacitance of a turn in the original helix. Equation (16) is based on an assumption that the mutual capacitance

between turns is negligible compared to the self capacitance of the wire. This is a reasonable assumption when the pitch angle satisfies the condition in Equation (4).

1.3 VALIDATION OF THE SIMPLIFIED MODEL

In order to validate the simplified model described in the previous sections, the input impedances and the radiation patterns of helical antennas and the corresponding simplified models were calculated using a full-wave numerical modeling tool [17]. Since a normal mode helical antenna is generally designed to operate at its resonant frequency, the performance of the simplified model near resonance is important. The evaluation was done by computing the relative differences in the calculated input resistance and resonant frequency. The error in the input resistance is defined as the ratio of the resistance difference over R_0, the input resistance of the helical antenna at its resonant frequency f_0. The error in the resonant frequency of the helical antenna is defined as the difference between the resonant frequency of the simplified antenna, f_1 f_1, and the full helix, f_0, divided by f_0. Expressed as a percentage, the equations for these errors are indicated below:

$$Error(\mathrm{Re}) = \frac{|R_0 - R|}{R_0} \times 100\% \tag{17}$$

$$Error(f) = \frac{|f_0 - f_1|}{f_0} \times 100\% \tag{18}$$

The geometrical parameters of the antennas evaluated are given in Table 1.1. The antennas are grouped in three sets. Within each set, one parameter was varied.

Table 1.1. Geometrical parameters of helical antennas.

No	Geometry	Resonant frequency
	Different wire radius	
1	$N=10, R=1$ mm, $S=1.68$ mm, $\alpha=15^{\circ}, a=0.01$ mm	2.89 GHz
2	$N=10, R=1$ mm, $S=1.68$ mm, $\alpha=15^{\circ}, a=0.02$ mm	2.97 GHz
3	$N=10, R=1$ mm, $S=1.68$ mm, $\alpha=15^{\circ}, a=0.04$ mm	3.08 GHz
	Different pitch angle	
4	$N=10, R=2$ mm, $S=2.67$ mm, $\alpha=12^{\circ}, a=0.02$ mm	1.47 GHz
5	$N=10, R=2$ mm, $S=4.57$ mm, $\alpha=20^{\circ}, a=0.02$ mm	1.38 GHz
6	$N=10, R=2$ mm, $S=10.5$ mm, $\alpha=40^{\circ}, a=0.02$ mm	1.00 GHz
	Different number of turns	
7	$N=10, R=2$ mm, $S=4.57$ mm, $\alpha=20^{\circ}, a=0.02$ mm	1.38 GHz
8	$N=20, R=2$ mm, $S=4.57$ mm, $\alpha=20^{\circ}, a=0.02$ mm	741 MHz
9	$N=40, R=2$ mm, $S=4.57$ mm, $\alpha=20^{\circ}, a=0.02$ mm	395 MHz

Table 1.2. Equivalent parameters of simplified models.

No	Equivalent parameters	*Error* (Re) (%)	*Error* (*f*) (%)
1	$a'=31.5a, L=6.21$nH	2.2	1.3
2	$a'=18.9a, L=5.35$nH	1.5	1.3
3	$a'=11.3a, L=4.51$nH	0.7	1.6
4	$a'=34.8a, L=13.2$nH	3.2	2.7
5	$a'=24.7a, L=11.5$nH	4.0	0.1
6	$a'=7.11a, L=9.07$nH	0.6	1.0
7	$a'=24.7a, L=11.5$nH	4.0	0.1
8	$a'=24.7a, L=11.5$nH	1.4	1.7
9	$a'=24.7a, L=11.5$ nH	3.2	2.2

The relative errors in the input resistance and resonant frequency for each case are listed in Table 1.2. The input resistances at the resonant frequency of the simplified model are in reasonable agreement (within 5%) with values calculated for the full helix in all cases. The good agreement suggests that the analytical formulas (13) - (16) are sufficiently accurate near resonance for the helical antenna geometries evaluated. Table 1.3 shows the computation time and the amount of memory per frequency required to

analyze each original helical antenna and its simplified model. The simplified model significantly reduces both the CPU-time and the memory usage.

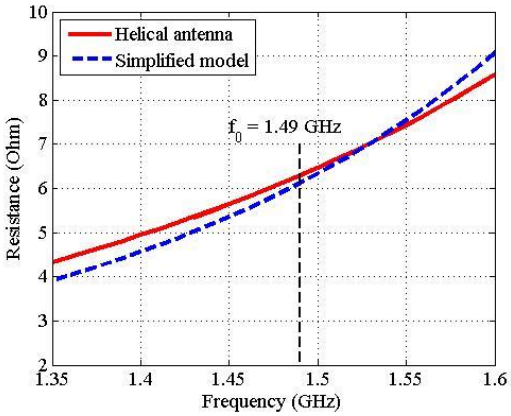

(a) Case 4: Input resistance.

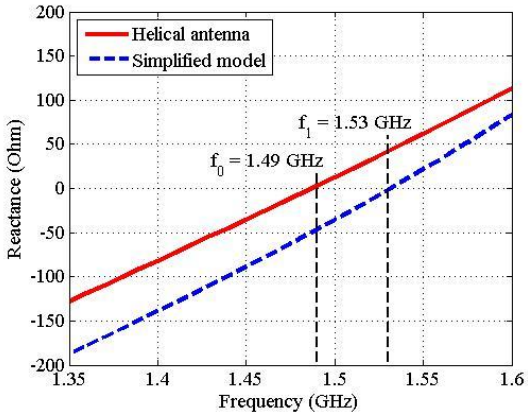

(b) Case4: Input reactance.

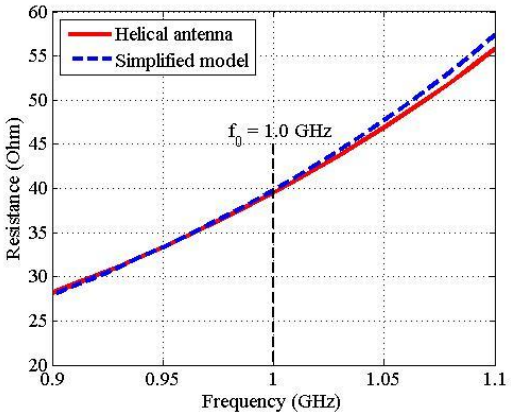

(c) Case 6: Input resistance.

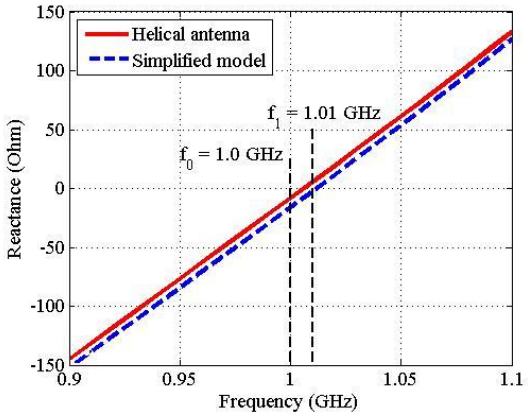

(d) Case 6: Input reactance.

Figure 1.3. Input impedance for Cases 4 and 6.

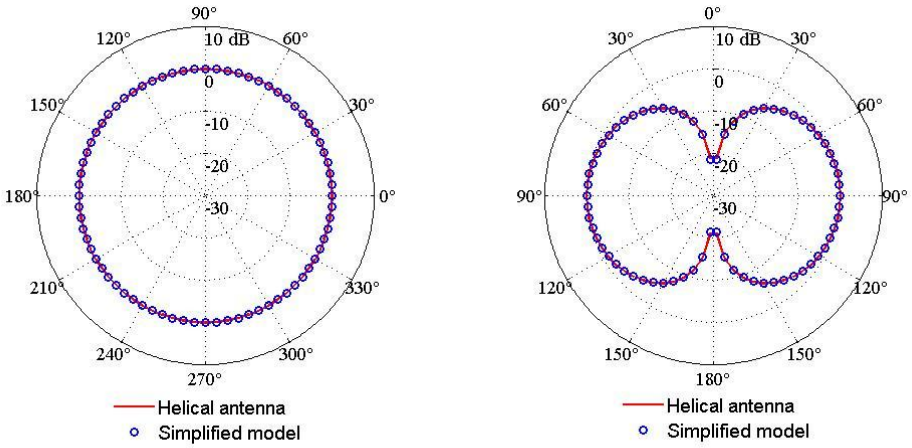

(a) (b)

Figure 1.4. Radiation patterns for Case 4: (a) Azimuth plane field pattern (b) Elevation plane field pattern.

Table 1.3. CPU-time and memory usage.

No	CPU-time (Second)		Memory-usage (MBtye)	
	Original model	Simplified model	Original model	Simplified model
1	4.28	0.4	14.8	0.54
2	4.23	0.65	14.8	0.75
3	4.95	0.64	16.9	0.96
4	20.8	0.46	65.6	0.72
5	24.9	0.46	74.4	0.82
6	44.3	2.37	115.5	2.8
7	24.9	0.43	74.4	0.82
8	146.4	1.51	311.3	2.67
9	506	5.42	890	9.54

One application of the simplified model is RFID antennas, which are widely used for identification and tracking of objects using radio waves. Recently, tire makers have begun embedding RFID tags in some of their tires to enable them to be tracked

electronically. These tags often employ helical antennas embedded in a dielectric material as illustrated in Figure 1.5. In this example, the antenna is designed to resonate at around 920 MHz. The parameters of the helix are: N = 106 turns, R = 0.5 mm, S = 0.833 mm, a = 0.09 mm. The dimensions of the dielectric block are 97 x 11 x 11 mm. The relative permittivity of the dielectric is 4.0.

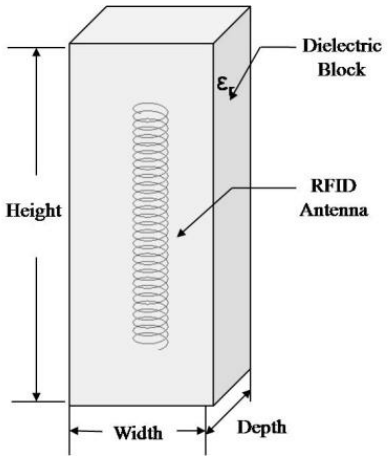

Figure 1.5. An RFID antenna embedded in a dielectric block.

The input impedance of both the RFID antenna and the simplified model are calculated for the antenna in air and the antenna in the dielectric block (Figure 1.6). The difference between the helix and simplified model calculations of the input impedance is less than 5% for both the RFID antenna in air and in the dielectric block.

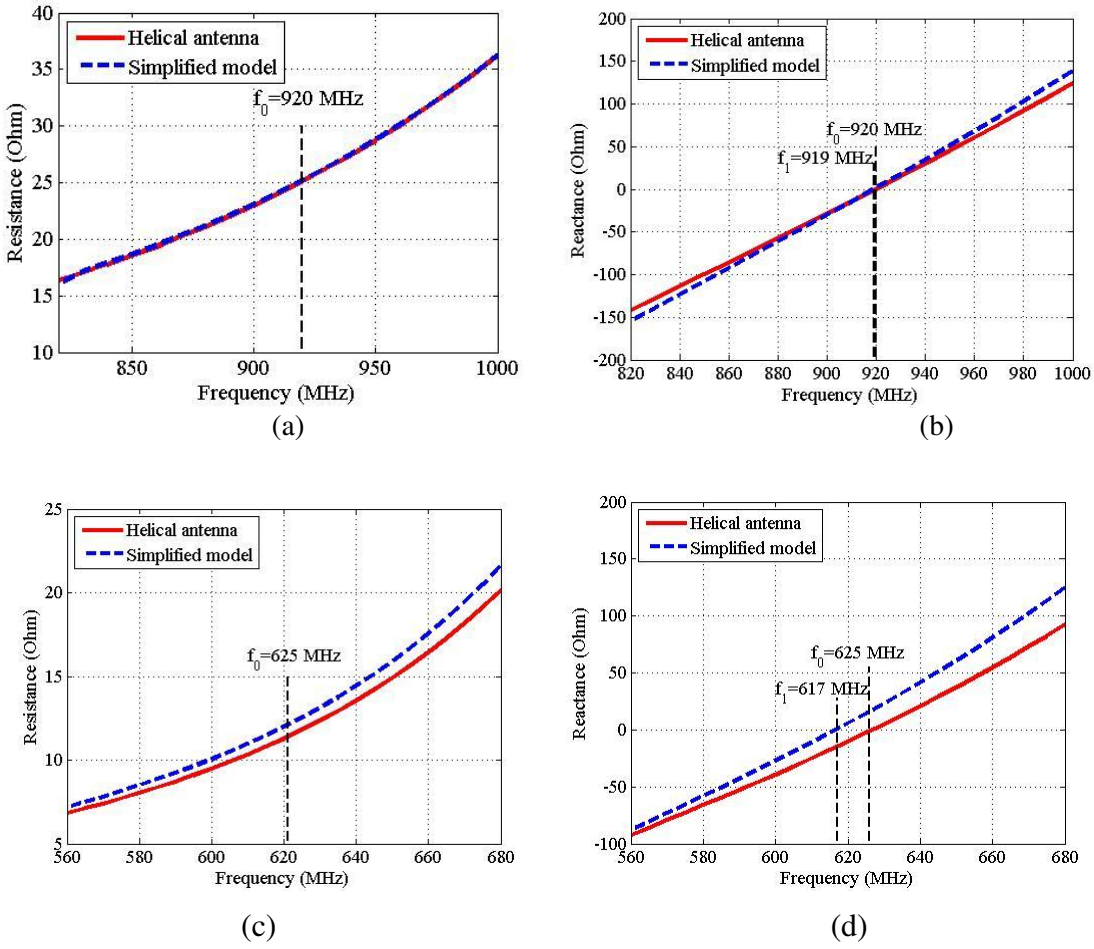

Figure 1.6. Input impedance of the RFID antenna and its simplified model: (a) Input resistance in air (b) Input reactance in air (c) Input resistance in dielectric (d) Input reactance in dielectric.

In order to further test the proposed model, a practical helical antenna design [3] for mobile handsets was also simulated. In this design, two helical antennas are mounted on top of a metal box (*10 x 4.8 x 1.67 cm*) and separated by 3.125 cm (Figure 1.7). Antenna 1 is excited and Antenna 2 is connected to a 50-Ω load. The helical antenna array is tuned to resonate at about 1.65 GHz. The antenna parameters are: N = 2.6 turns, S

= 9.94 mm, R = 2.1 mm, a = 0.28 mm. The simplified model requires an integer number of turns. Therefore, the number of turns was set to 3 in this simulation.

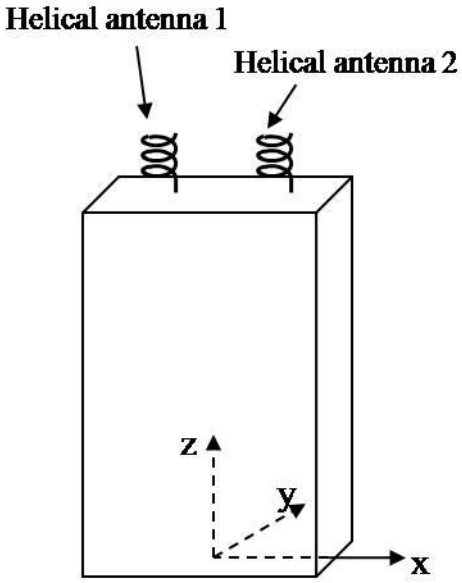

Figure 1.7. Mobile handset and coordinate system.

The simulation results are shown in Figures 1.8 and 1.9. The input resistance of the simplified model is close to that of the helical antenna near the resonant frequency. The error in the resonant frequency is only 1%. The radiation pattern predicted by the simplified model is identical to that of the helical antenna in both azimuth and elevation planes. The good agreement demonstrates that the proposed model is not only suitable for dipole-helical antennas, but it can be also applied to monopole-helical antennas.

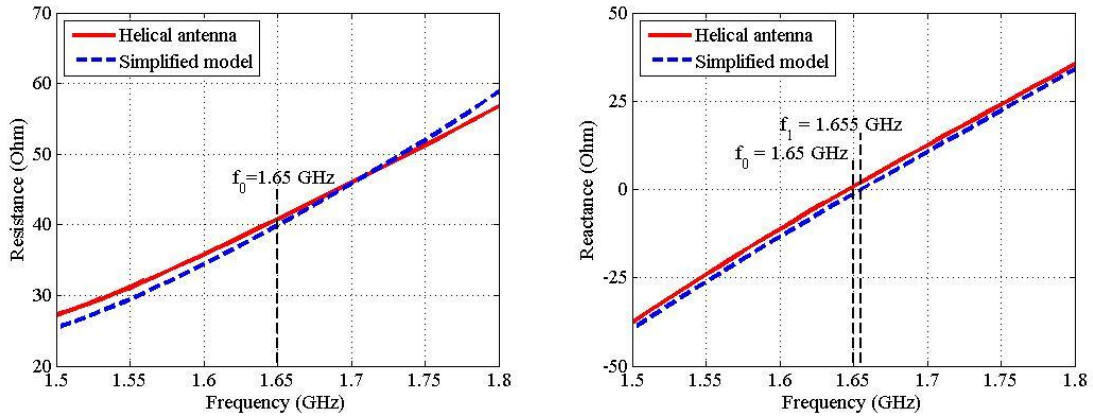

(a) (b)

Figure 1.8. Input impedance of the helical antenna of the handset: (a) Input resistance (b) Input reactance.

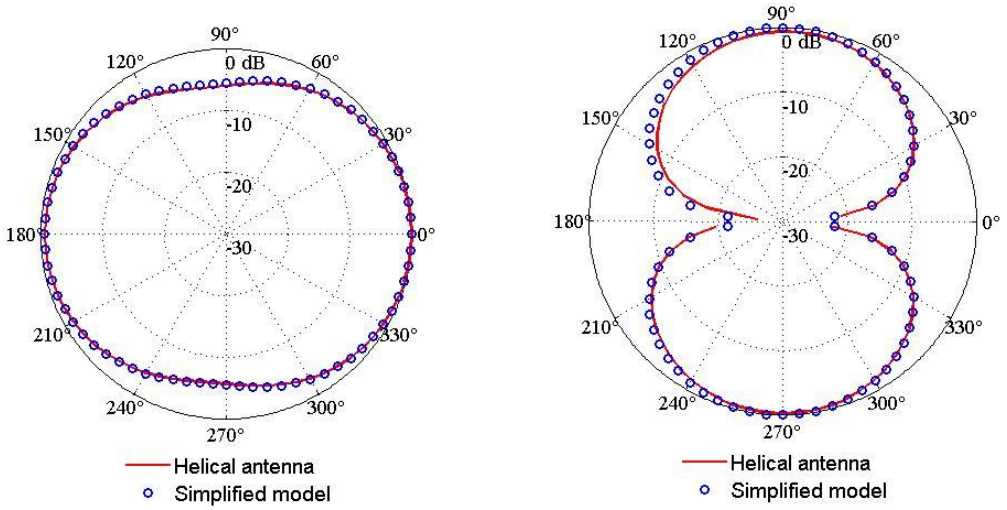

(a) (b)

Figure 1.9. Radiation patterns for the handset helical antenna in the Azimuth plane: (a) E_θ (b) E_φ.

1.4 CONCLUSIONS

A simplified model for helical antennas has been proposed. In the model, the highly curved structure of the helix is replaced with a straight-wire and inductor structure. The number of elements required to model the helix is significantly reduced; and therefore, analysis of the simplified model uses much less computational resources than analysis of the full helix.

REFERENCES

[1] J. D. Kraus, *Antennas*, 2nd ed., McGraw-Hill, 1988.

[2] Y. Hiroi, K. Fujimoto, "Practical usefulness of normal mode helical antenna," *IEEE AP-S Int. Symp*., pp. 238-241, 1976.

[3] H. T. Hui, "Practical dual-helical antenna array for diversity/MIMO receiving antennas on mobile handsets," *IEE Proceeding, Microwaves, Antennas and Propagation*, vol. 152, no. 5, pp. 367-372 2005.

[4] M. M. Faiz and P. F. Wahid, "Microstrip line matched normal mode helical antenna for cellular communication," *Southeastcon'98, Proceedings, IEEE*, pp. 182-185.

[5] H. Morishita, Y. Kim, H. Furuuchi, K. Sugita, Z. Tanaka and K. Fujimoto, "Small balance-fed helical dipole antenna system for handset," *51st Vehicular Technology Conference (VTC) Proceedings*, Tokyo, vol. 2, pp.1377 – 1380, May 15-18, 2000.

[6] K. Noguchi, S. Betsudan, T. Katagi, and M. Mizusawa, "A compact broad-band helical antenna with two-wire helix," *IEEE Trans. Antennas Propagat*., vol. 51, no. 9, pp. 2176-2181, 2003.

[7] Y. Yamada, W. G. Hong, W. H. Jung and N. Michishita, "High gain design of a very small normal mode helical antenna for RFID tags," *IEEE Region 10 Conference*, pp. 1-4, 2007.

[8] A.R. Djordjevic, A.G. Zajic, M.M. Ilic, and G.L. Stuber, "Optimization of helical antennas," *IEEE Trans. Antennas Propagat*., vol. 48, pp. 107-105, 2007.

[9] G. Lazzi, and O. P. Gandhi, "On modeling and personal dosimetry of cellular telephone helical antennas with the FDTD codes," *IEEE Trans. Antennas Propagat*., vol. 46, pp. 525-530, 1998.

[10] E. D. Caswell, "Analysis of a helical antenna using a moment method approach with curved basis and testing functions," M. Sc. Thesis, Virginia Polytechnic Institute, 1998.

[11] C. A. Balanis, *Antenna Theory – Analysis and Design*, 3rd ed., John Wiley & Sons Inc., 2005.

[12] S. Ramo, J. R. Whinnery and T. V. Duzer, *Fields and Waves in Communication Electronics*, New York, J. Wiley, 1965.

[13] S. A. Schelkunoff and H. T. Friis*, Antennas: Theory and Practice*, John Wiley & Sons Inc., 1952.

[14] F. M. Tesche, et al., EMC *Analysis Methods and Computational Models*, Wiley-IEEE, 1997.

[15] A. J. Palermo, "Distributed capacity of single layer coils", *Proc. IRE*, vol. 22, pp.897-903, 1934.

[16] G. H. Brown and O. M. Woodward, Jr., "Experimentally determined impedance characteristics of cylindrical antennas," *Proc. IRE*, vol. 33, pp. 257-262, 1945.

[17] FEKO, http://www.feko.info.

CHAPTER TWO

IMBALANCE DIFFERENCE MODEL FOR COMMON-MODE RADIATION FROM PRINTED CIRCUIT BOARDS

Changyi Su and Todd Hubing

ABSTRACT

The differential-mode signals in printed circuit board (PCB) traces are unlikely to produce significant amounts of radiated emissions directly; however these signals may induce common-mode currents on attached cables, enclosures or heatsinks that result in radiated electromagnetic interference. Full-wave EM modeling can be performed in order to determine the level of radiated emissions produced by a PCB, but this modeling is computationally demanding and doesn't provide the physical insight necessary to explain how differential signals induce common-mode currents on distant objects. This paper describes a model for determining the common-mode currents on cables attached to a PCB that is based on the concept of *imbalance difference*. The imbalance difference model is derived from research that shows that changes in geometrical imbalance cause differential- to common-mode conversion. This paper applies an imbalance difference model to PCB structures and compares the resulting equivalent source configurations to those obtained with traditional voltage- and current-driven models as well as full structure simulations.

2.1 INTRODUCTION

Common-mode currents are much more likely to generate significant levels of unintentional radiated emissions than differential-mode currents [1]. Signal traces on PCBs carry differential currents by design, but the signals on these traces can couple to larger nearby objects such as heatsinks, enclosures and attached cables. The common-mode currents induced on these objects can be significant sources of radiated emissions.

For simple PCB structures, the radiated emissions can be calculated using full-wave numerical modeling codes. However, this approach is limited by the complex models and extensive computational resources required to analyze the details of each trace structure. In addition, brute-force modeling of the entire board provides relatively little physical insight into the electromagnetic interference (EMI) source mechanisms. Alternatively an effective equivalent model can be obtained by eliminating sources and differential signal structures that do not contribute significantly to the radiated emissions and focusing on the features that could possibly be significant sources of EMI. Equivalent models are generally much simpler than model-everything full-wave models and provide physical insight into the board features that have the greatest impact on radiated emissions.

Two equivalent models analyzing the differential-mode to common-mode conversion in PCBs were introduced in a 1994 paper by Hockanson [2]. These models are commonly referred to as current-driven and voltage-driven sources, referring to the prominent differential signal parameter affecting the common-mode currents induced on the external structures. The current-driven mechanism refers to common-mode currents

induced by the signal currents returning in the "ground" structure causing voltage differences between objects referenced to different parts of the structure [2]-[4]. The voltage-driven mechanism refers to electric-field coupling from traces or heatsinks that are at one potential to cables or other external objects that are at a different potential [5]-[7]. An equivalent wire antenna model for estimating voltage-driven common-mode currents was developed in [5]. In this model, the common-mode voltage source is placed at the junction between the ground plane and the attached cable. The magnitude of the equivalent voltage source is expressed in terms of the ratio of the self-capacitances of the board and the trace or heatsink.

These equivalent models are typically applied in situations where it is assumed that one coupling mechanism is dominant. However, for trace-and-board geometries, common-mode currents due to the electric and the magnetic field coupling coexist and can be comparable in strength. Therefore, it is desirable to model the coupling between the differential signals on the board and the common-mode currents on attached cables without specifying a particular field coupling mechanism. In the work presented here, an equivalent model based on the concept of imbalance difference [8, 9] is described. The imbalance difference model is another way of describing how differential-mode signals are converted to common-mode voltages and currents, based on changes in the degree of imbalance in PCB transmission systems. Using a parameter called the *current-division factor* or *imbalance parameter*, the magnitude and location of equivalent common-mode sources can be derived quantitatively. These common-mode sources then replace all of the differential signal structures on the PCB. This paper demonstrates the application of

the imbalance difference model to PCB circuit structures and compares the models obtained to current- and voltage-driven models and to full-wave simulations of the entire board structure.

2.2 DESCRIPTION OF THE IMBALANCE DIFFERENCE

In 2000, a paper by Watanabe demonstrated that geometrical imbalance in a circuit does not necessarily result in differential-mode to common-mode conversion. Instead, it was proposed that *changes* in the imbalance are responsible. Watanabe introduced a method for quantifying the imbalance in a given transmission line structure and showed that it was possible to characterize the differential- to common-mode conversion by introducing equivalent common-mode voltage sources at points where there was a change in the imbalance. This idea was subsequently developed in a number of other publications [10]-[15] and has proven to be a powerful tool for the design and modeling of PCB structures.

In order to illustrate how this concept can be applied to PCBs with attached cables, consider the structure shown in Figure 2.1. Figure 2.1 schematically shows a simple circuit board structure with a signal trace routed over a solid ground plane. The board has cables attached to both ends that are referenced to the ground plane. The microstrip trace is driven at one end and terminated at the other end. The trace-board geometry is electrically small at low frequencies where common-mode currents induced on the cables are likely to be the dominant source of radiated emissions. The space between the trace and the ground plane is filled with a dielectric material with a dielectric

constant, ε_r, and a thickness, t. In Figure 2.1, the thickness, t, is exaggerated for clarity. In most practical structures, t is several orders of magnitude smaller than L and W.

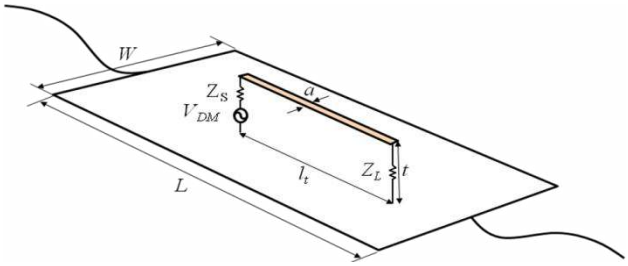

Figure 2.1. A trace-board structure with cables attached to the ground plane.

An imbalance parameter can be defined for any transmission line geometry. The imbalance parameter is a number between 0 and 0.5, where a perfectly balanced structure (e.g. two symmetric conductors with identical cross sections) has an imbalance parameter of 0.5. Perfectly unbalanced structures (e.g. a coaxial cable or a trace over an infinite ground plane) have imbalance parameters equal to 0. The imbalance parameter, denoted as "h" in this paper, is dependent on the cross-sectional structure of the transmission line and therefore changes when two transmission lines with different cross-sections are connected.

The change in the imbalance at the interconnection can be used define an equivalent common-mode voltage source for the purpose of modeling the common-mode currents induced on the structure. Using Figure 2.2 as an example, there is a change in the imbalance parameter, h, at both ends of the microstrip. At each end, the width of the trace varies from a finite value, a, to zero. At the discontinuity points A and B, as shown in

Figure 2.2 (a), common-mode voltages are generated in the ground plane and their magnitudes are computed as the product of the differential-mode voltage and the change in the imbalance parameter [9],

$$\Delta V_C(x) = \Delta h V_N(x) \tag{1}$$

where V_N is the differential-mode voltage between the signal trace and the return plane, and x denotes the location of the common-mode excitation. According to (1), the common-mode excitation at location A is computed by,

$$\Delta V_C(A) = \left(h_2 - h_1\right) V_N(A) \tag{2}$$

and the common-mode excitation at B is

$$\Delta V_C(B) = \left(h_3 - h_2\right) V_N(B) \tag{3}$$

The common-mode equivalent geometry is excited by $\Delta V_c(A)$ and $\Delta V_c(B)$, which are placed on the board at points A and B, respectively, as shown in Figure 2.2(b).

As indicated in (2) and (3), the relationship between the differential-mode and common-mode source amplitudes is completely determined by the change of the imbalance parameter. The imbalance parameter, h, is defined as,

$$h = \frac{I_{CM-signal}}{I_{CM}} \tag{4}$$

where I_{CM} and $I_{CM\text{-}signal}$ are the total common-mode current and the common-mode current flowing on the signal trace, respectively. For microstrip trace structures, this parameter is given by [12],

$$h = \frac{C_{trace}}{C_{trace} + C_{board}} \tag{5}$$

where C_{trace} and C_{board} are the stray capacitances per unit length of the signal trace and the ground plane, respectively. Stray capacitance does not include the mutual capacitance between the trace and ground plane and is represented by the lines of electric flux that originate on the trace or the board and terminate at infinity. Equation (5) was derived from the telegrapher's equations with the assumption that only the TEM mode propagates on each transmission line. The line capacitances per unit length can be extracted numerically using a two-dimensional electrostatic or quasi-static code. In this paper, QuickField Students' version [16], a free two-dimensional finite element code, was used to compute the capacitances in all simulations presented in Section 2.4.

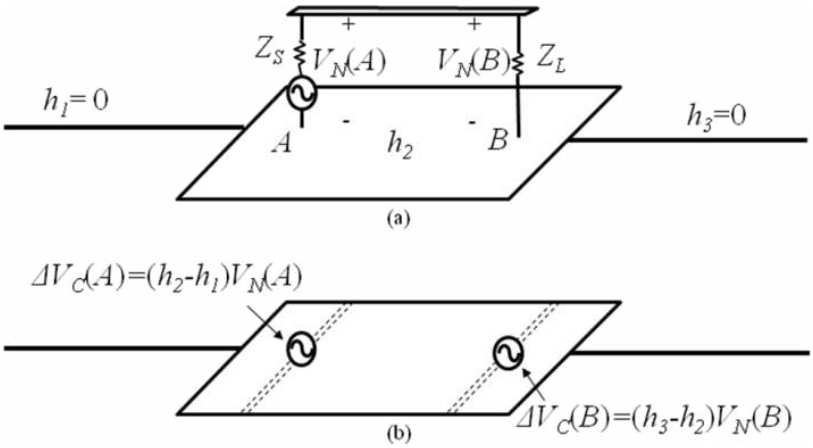

Figure 2.2. Imbalance difference model: (a) trace-and-board configuration (b) equivalent model.

The imbalance parameter for the portions of the structure extending beyond the

trace is zero. The imbalance parameter for the trace-board portion, h_2, must always be between zero and one. Since h_1 and h_3 are zero, the common-mode voltages in (2) and (3) can be rewritten as,

$$V_{CM}(A) = h_2 V_N(A) \tag{6}$$

and

$$V_{CM}(B) = -h_2 V_N(B) \tag{7}$$

An important restriction on the use of this modeling approach is that the cross-section of the board-trace configuration must be small relative to a wavelength; otherwise, the imbalance factor is not well defined. This restriction also applies to traditional voltage- and current-driven models.

2.3 IMBALANCE DIFFERENCE COMPARED TO VOLTAGE- AND CURRENT-DRIVEN MODELS

2.3.1 Imbalance Difference Model for the Trace-board Configuration

Figure 2.3 illustrates the imbalance difference model for the trace-board configuration of Figure 2.1 after the trace and differential-mode source have been replaced by the equivalent common-mode sources. Expressed as a function of the trace current, the magnitude of the differential-mode voltage between the trace and the ground plane at point *A* in Figure 2.1 is,

$$V_N(A) = \left| j2\pi f L_{trace} I_{DM} + Z_L I_{DM} \right| \tag{8}$$

Combining (5), (6) and (8), the equivalent common-mode voltage at point *A* is,

$$V_1 = \left| jh2\pi f L_{trace} I_{DM} + hZ_L I_{DM} \right| \tag{9}$$

where I_{DM} is the differential-mode current. Taking the differential-mode current as a reference, the phasor expression for the common-mode voltage is

$$\begin{aligned}\mathbf{V_1} &= 2\pi f L_{trace} I_{DM} \angle 90^\circ + h Z_L I_{DM} \angle 0^\circ \\ &\approx h 2\pi f I L_{trace\,DM} \angle 90^\circ + h \frac{Z_L}{Z_S + Z_L} V_{DM} \angle 0^\circ\end{aligned} \tag{10}$$

Similarly, the equivalent common-mode voltage at point B is given by

$$V_2 = h \frac{Z_L}{Z_S + Z_L} V_{DM} \tag{11}$$

Figure 2.3. Imbalance difference model for the trace-board configuration in Figure 2.1.

From (10) and (11), the equivalent model consists of two parts. One part is the first term in (10), which is proportional to the differential-mode current. The other part is the second term in (10) and (11), which is proportional to the differential-mode voltage.

2.3.2 Voltage- and Current-driven Models for the Trace-board Configuration

It is interesting to compare the imbalance difference model to a combination of the current-driven model [3] and the voltage-driven model [5] as shown in Figure 2.4. In the current-driven model, one equivalent voltage source is placed at the midpoint of the current return path on the board. The magnitude of the source is proportional to the differential-mode current flowing through the trace,

$$V_1 = 2\pi f L_{return} I_{DM} \tag{12}$$

where L_{return} is the partial inductance of the return plane [4]

$$L_{return} = \frac{\mu_0}{\pi}\frac{tl_t}{W}\frac{1}{\sqrt{1-4(1-2t/W)(s/W)^2}} \tag{13}$$

s is the offset of the trace from the center of the board, and t, l_t, W are the trace height , the trace length and the board width as shown in Figure 2.1, respectively.

In the voltage-driven model, equivalent voltage sources are placed at the junctions between the cables and the plane. The magnitudes of the voltage sources are expressed in terms of the ratio of the self-capacitances of the board and the trace,

$$V_2 = V_3 = \frac{C_{trace}}{C_{board}}\frac{Z_L}{Z_S + Z_L}V_{DM} \tag{14}$$

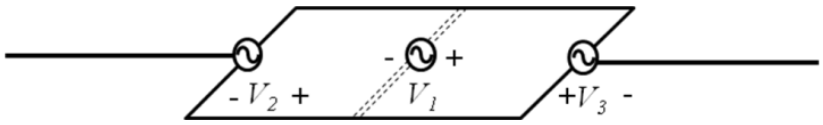

Figure 2.4. Equivalent model based on the current and voltage-driven models.

Although the two equivalent models (Figures. 2.3 and 2.4) differ in the number, the locations, and the magnitudes of the equivalent sources, they are both approximately equivalent to the original trace-board configuration. It is demonstrated in the next section that the predicted radiated emissions using the two models produce similar results at frequencies up to 500 MHz.

2.3.3 Equivalent models for Shorted and Open Trace Configurations

A shorted-trace configuration is a special case of Figure 2.2(a) that enhances the current-driven coupling and suppresses the voltage-driven coupling to the cables.

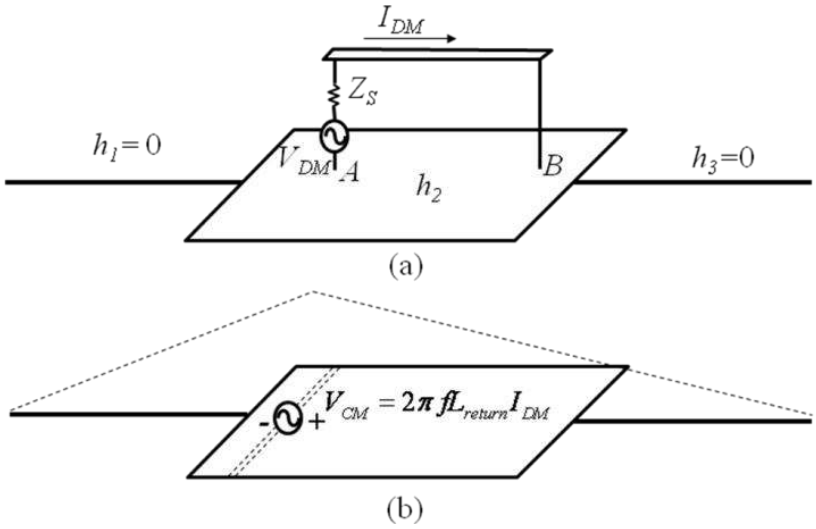

Figure 2.5. Imbalance difference model for the shorted trace structure.

At point *A*, the equivalent common-mode voltage is given by (2),

$$V_{CM} = h_2 V_N(A) = \frac{C_{trace}}{C_{trace} + C_{board}} 2\pi f L_{trace} I_{DM} \tag{15}$$

The loop inductance causes the differential current I_{DM} to lag the differential-mode voltage V_{DM}. Assuming the phasor of the differential current is $I_{DM}\angle 0^\circ$, the common-mode voltage in (15) can be expressed using phasor notation as,

$$\mathbf{V_{CM}} = 2\pi f L_{trace} \frac{C_{trace}}{C_{trace} + C_{board}} I_{DM}\angle 90^\circ \tag{16}$$

The trace is shorted to the ground plane at the load side; so according to (3), the

magnitude of the equivalent common-mode excitation at point *B* is zero,

$$\Delta V_C(B) = -h_2 V_N(B) = 0 \tag{17}$$

To enhance the voltage-driven coupling and suppress the current-driven coupling to the cables, the load end of the trace is open-circuited as shown in Figure 2.6(a). Since the imbalance parameter is independent of the loading condition, (5) is still valid for the open-circuit case. Therefore, the magnitude of the equivalent common-mode voltage is,

$$V_{CM} = \frac{C_{trace}}{C_{trace} + C_{board}} V_{DM} \tag{18}$$

Two common-mode voltage sources are placed on the return plane. Those sources have the same magnitude but opposite phase.

The equivalent antenna model for the open-circuit geometry is shown in Figure 2.6(b).

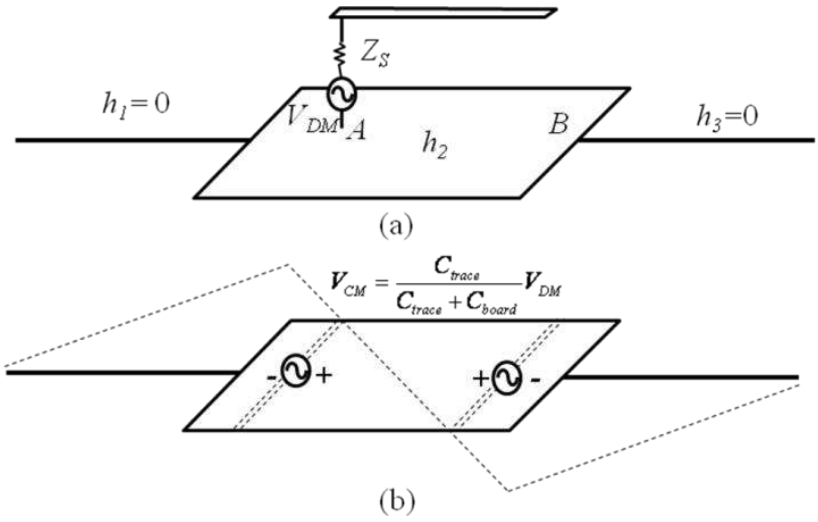

Figure 2.6. Imbalance difference model for the open-circuit structure.

In the imbalance difference model of the open-circuit geometry, two common-mode voltage sources are placed at points *A* and *B*, respectively. They have the same magnitude but opposite phases. Hence, the common-mode current distribution is mirrored across the center of the board.

It is noted that the current-driven mechanism induces common-mode currents that flow in the same direction on the two cables, while the voltage-driven mechanism induces common-mode currents that flow in opposite directions on the two cables. Therefore, when both mechanisms are significant, the total common-mode current will not be the same on both wires.

2.4 MODELING EXAMPLES

2.4.1 Trace Terminated with 50 ohms

To evaluate the imbalance difference models described in the previous section, numerical simulations of the trace-board configuration in Figure 2.1 were performed. The maximum radiated electric fields at a distance of 3 meters were calculated for both the original configuration (modeling the entire trace-board structure) and the equivalent common-mode models (i.e., the imbalance difference model, current-driven model and voltage-driven model). The simulations were performed using a full-wave electromagnetic modeling code based on the method of moments [17].

The board dimensions were 10 cm x *W* cm, where *W* was the width of the board. A 5-cm long, 1-mm wide trace was placed 3 mm above the plane, and two 50-cm cables were attached to the board and oriented horizontally. A 2-V source with a 50-Ω series impedance was connected between one end of the trace and the ground plane. The other

end of the trace was terminated by a 50-ohm resistor. The board was located in free space.

Figure 2.7 shows the maximum radiated electric fields obtained from 4-cm and 10-cm wide boards. The solid curves include the maximum radiation obtained from a full-wave model of the entire configuration. As indicated by (5), the imbalance parameter can be reduced by widening the ground plane. Hence, the common-mode radiated emissions from the 10-cm wide board are about 8 dB lower than the emissions from the 4-cm wide board. This observation is consistent with the experimental results in [3].

In Figure 2.7, the dashed lines and dash-dot lines represent the results obtained from the imbalance difference model in Figure 2.3 and the voltage/current-driven model in Figure 2.4, respectively. Both equivalent models yield results that are in reasonable agreement with the original configuration, particularly near the resonant peaks.

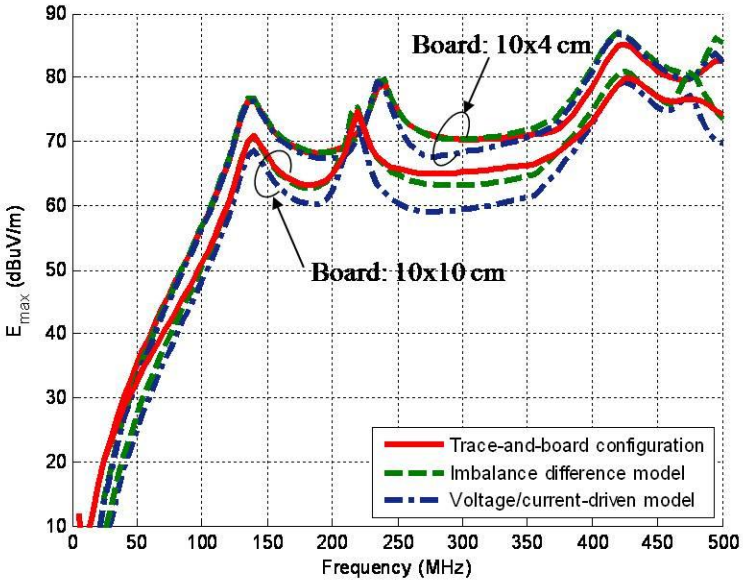

Figure 2.7. Comparison of the radiated emissions from the full trace-board configuration and the two equivalent models.

2.4.2 Trace Terminated with 0 ohms

The imbalance difference model eliminates the need to make assumptions about which source model is dominant in a given situation. To illustrate the value of this, the geometry in the previous section was modeled with the trace shorted to the ground plane at the load. The source amplitude was 2 V and the source impedance was 100 ohms. This is a configuration where the current-driven mechanism might be expected to dominate. The current is approximately the same as it was in the 50-ohm load configuration, but the voltage is significantly reduced.

The maximum 3-meter radiation from 4-cm and 10-cm wide boards was calculated using the imbalance difference model and compared to results obtained by analyzing the original trace-board configuration. The emissions from the shorted-trace configuration are shown in Figure 2.8(a). The solid line is the result obtained from analysis of the complete trace-board structure. The dashed line represents the simulation result for the imbalance difference model. The magnitude of the equivalent common-mode voltage was computed using (15). Figure 2.8(b) compares the maximum electric field radiated from the open-circuited board using both the original model and the imbalance difference model. In this case, the magnitudes of the equivalent common-mode excitations were computed using (18).

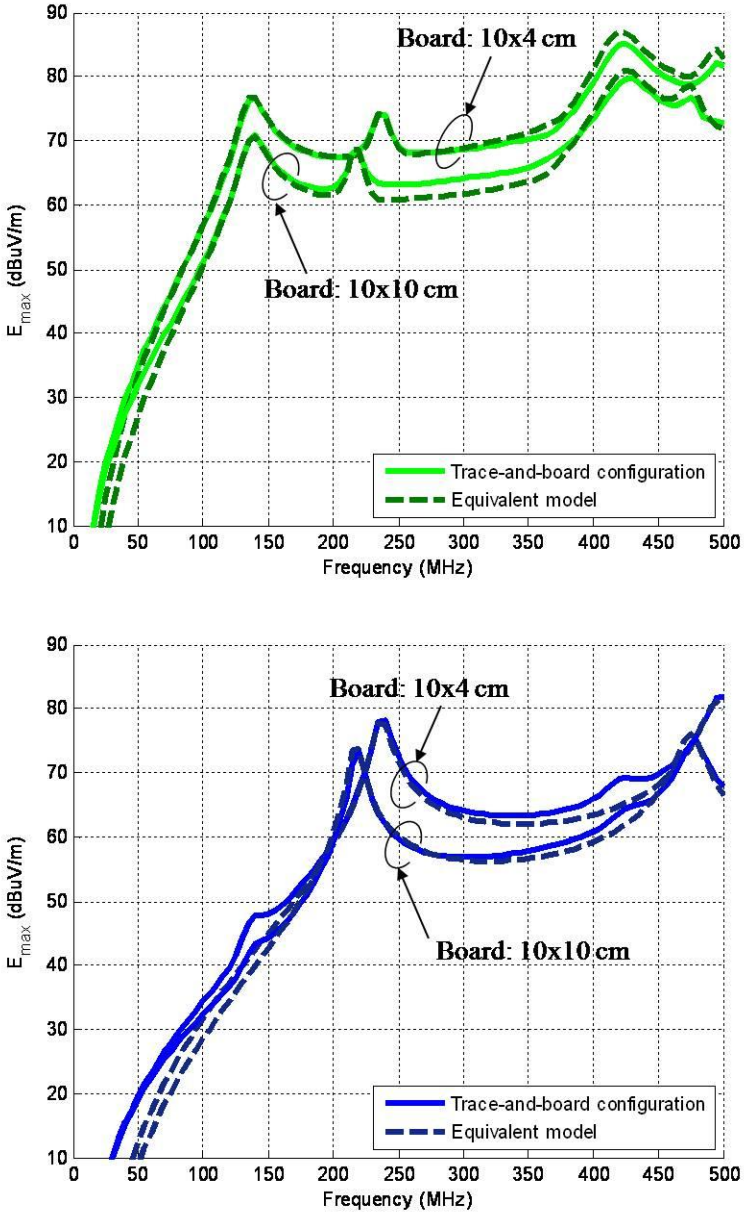

Figure 2.8. Comparison of the radiated emissions calculated using the trace-board configuration and the imbalance difference model from shorted trace (upper plot) and open trace (lower plot).

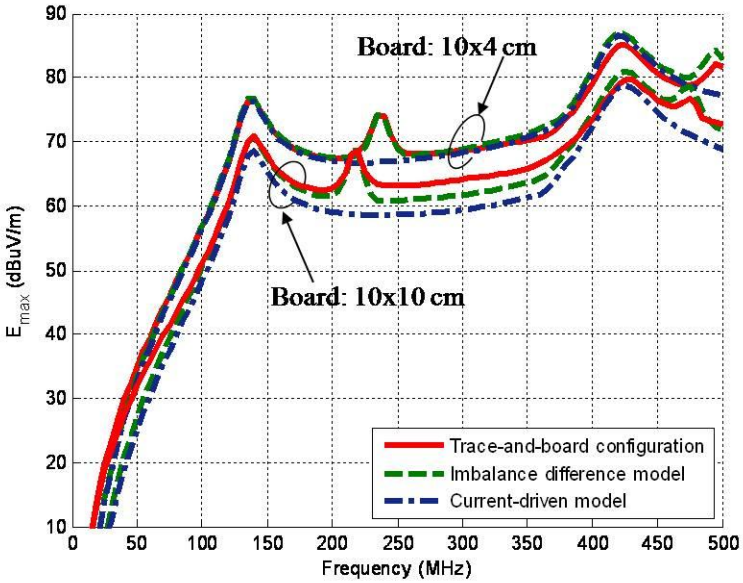

Figure 2.9. Comparison of the radiated emissions from the shorted-trace configuration calculated using the imbalance difference model and current-driven model.

The simulation results in Figure 2.9 show that both the imbalance model and the current-driven model calculate the maximum radiation from the shorted-trace configurations with reasonable accuracy. However, the current-driven model fails to predict the small peaks at 235 MHz and 495 MHz for the 10 x 4 cm boards, and at 215 MHz and 475 MHz for the 10 x 10 cm boards. Further analysis shows that these peaks are caused by the voltage difference between the trace and the ground plane, which is zero at the load, but non-zero away from the load due to the inductance of the trace. Although the current-driven peaks are dominant, the voltage-driven mechanism cannot be neglected, even when the signal trace is shorted to the ground plane.

2.4.3 Trace Located Near the Board Edge

It has been demonstrated experimentally and through numerical modeling that the radiated fields are higher when signal traces are located near the board edge. Berg *et. al*. [18] explained that the increment in the radiated emissions is the result of increased magnetic flux beneath the board. Explained in terms of the imbalance difference model described in Section 2.3, the imbalance parameter of the trace-board pair increases as the trace is moved towards the board edge.

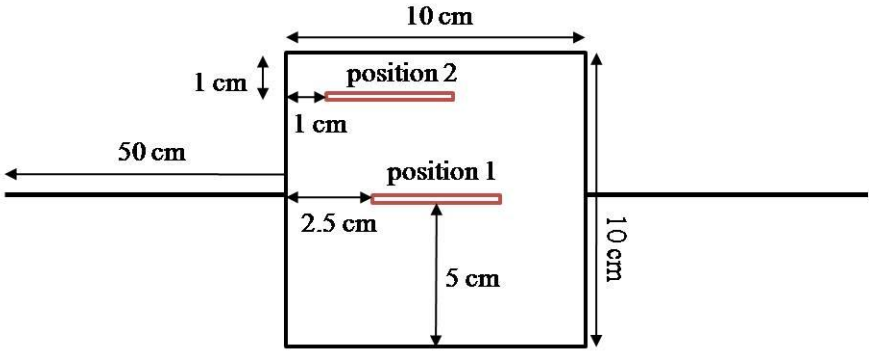

Figure 2.10. Test board configuration with different trace positions.

To illustrate this, boards were evaluated with different trace positions. Figure 2.10 shows a 10 cm x 10 cm board with a cable attached to each side. A 1-mm wide, 5-cm long trace is located 3 mm above the ground plane. Two different trace positions were evaluated. The maximum radiated fields from the board are shown in Figure 2.11. The simulation results show that the radiated field is stronger when the trace is near the board edge. The imbalance parameter is 0.0236 for the trace at position 1 and 0.0341 for the trace at position 2; resulting in a 5 dB difference at 220 MHz. The imbalance difference

model results are similar to the full trace-and-board configuration results over the entire frequency range evaluated.

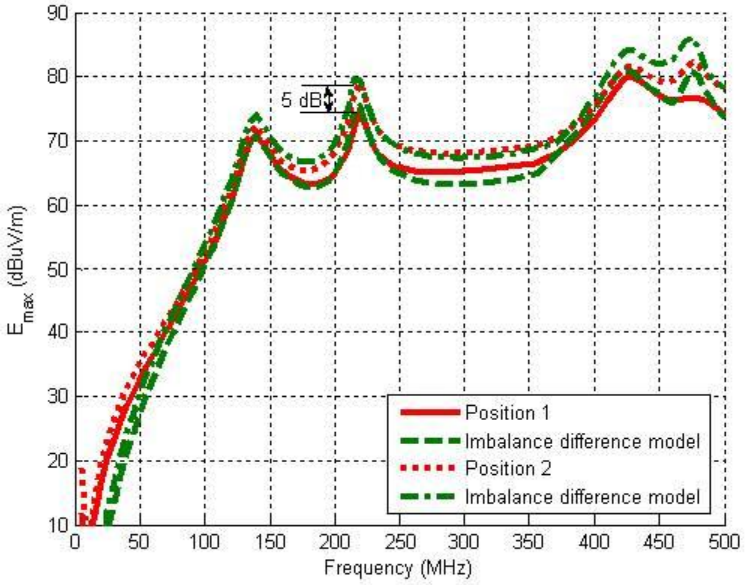

Figure 2.11. Comparison of radiated fields from the full trace-board configuration and the imbalance difference model for two trace positions.

2.5 CONCLUSIONS

The imbalance difference model can be used to estimate the radiated emissions from trace-board structures due to common-mode currents induced on attached cables. The results obtained are similar to results obtained using voltage- and current-driven models. Both models produce accurate results even though they employ equivalent sources that have different amplitudes and locations. The voltage- and current-driven models have the advantage that they are more intuitively linked to the field coupling responsible for the induced currents. However, by observing the amplitudes of the terms

in (10) and (11), the imbalance difference model also provides useful information about the relative importance of the electric and magnetic field coupling. Furthermore, the imbalance difference model has the advantage that is simpler to implement and models both electric and magnetic field coupling simultaneously.

REFERNCES

[1] C. R. Paul, *Introduction to Electromagnetic Compatibility*, John Wiley & Sons, New York, 1992.

[2] J. L. Drewniak, T. H. Hubing, and T. P. Van Doren, "Investigation of fundamental mechanisms of common-mode radiation from printed circuit boards with attached cables," in *Proc. IEEE Int. Symp. Electromagn. Compat.*, Chicago, IL, Aug. 1994, pp. 110-115.

[3] D. M. Hockanson, J. L. Drewniak, T. H. Hubing, T. P. Van Doren, F. Sha, and M. Wilhelm, "Investigation of fundamental EMI source mechanisms driving common-mode radiation from printed circuit boards with attached cables," *IEEE Trans. Electromagn. Compat*., vol. EMC-38, no. 4, pp. 557-566, Nov. 1996.

[4] M. Leone, "Design expressions for trace-to-edge common-mode inductee of a printed circuit board," *IEEE Trans. Electromagn. Compat*., vol. 43, no. 4, pp. 667-671, Nov. 2001.

[5] H. Shim and T. Hubing, "Model for estimating radiated emissions from a printed circuit Board with attached cables driven by voltage-driven sources," *IEEE Trans. Electromagn. Compat*., vol. 47, no. 4, pp. 899-907, Nov. 2005.

[6] H. Shim and T. Hubing, "Derivation of a closed-form expression for the self-capacitance of a printed circuit board trace," *IEEE Trans. Electromagn. Compat*., vol. 47, no. 4, pp. 1004-1008, Nov. 2005.

[7] S. Deng, T. Hubing and D. Beetner, "Estimating maximum radiated emissions from printed circuit boards with an attached cable," *IEEE Trans. Electromagn. Compat*., vol. 50, no. 1, pp. 215-218, Feb. 2008.

[8] T. Watanabe, O. Wada, T. Miyashita and R. Koga, "Common-mode-current generation caused by difference of unbalance of transmission lines on a printed circuit board with narrow ground pattern," *IEICE Transactions on Communications*, vol. E83-B, no. 3, March 2000, pp. 593-599.

[9] T. Watanabe, O, Wada, Y. Toyota, and R. Koga, "Estimation of common-mode EMI caused by a signal line in the vicinity of ground edge on a PCB," in *Proc. IEEE Int. Symp. Electromagn. Compat.*, Minneapolis, Aug. 2002, pp.113-118.

[10] T. Watanabe, et al., "Equivalence of two calculation methods for common-mode excitation on a printed circuit board with narrow ground plane," in *Proc. IEEE Int. Symp. Electromagn. Compat.*, Boston, MA, Aug. 2003, pp. 22-27.

[11] O. Wada, "Modeling and simulation of unintended electromagnetic emission from digital circuits," *IEICE Transactions on Communications* (Japanese Edition), vol. 87, no. 8, pp. 1062-1069, July 2003.

[12] T. Watanabe, H. Fujihara, O. Wada, Y. Toyota, R. Koga, and Y. Kami, "A prediction method of common-mode excitation on a printed circuit board having a signal trace near the ground edge," *IEICE Trans. Commun*. vol. E87-B, no. 8, Aug. 2004.

[13] Y. Toyota, et al., "Prediction of electromagnetic emissions from PCBs with interconnections through common-mode antenna model," in *Proc. IEEE Int. Symp. Electromagn. Compat.*, Zurich, Sept. 2007, pp. 107-110.

[14] Y. Toyota, T. Matsushima, K. Iokibe, R. Koga, T. Watanabe, "Experimental validation of imbalance difference model to estimate common-mode excitation in PCBs," in *Proc. IEEE Int. Symp. Electromagn.Compat.*, Detroit, Aug. 2008, pp. 1-6.

[15] T. Matsushima, T. Watanabe, Y. Toyota, R. Koga, and O. Wada, "Evaluation of EMI reduction effect of guard traces based on imbalance difference model," *IEICE Trans. Commun*., vol. E92-B, no. 6, June, 2009.

[16] QuickField Students' version 5.6, http://www.quickfield. com/free_soft. htm.

[17] FEKO User's Manual, Suite 5.5, July 2009.

[18] D. Berg, M. Tanaka, Y. Ji, X. Ye, J. Drewniak, T. Hubing, R. DuBroff, and T. Van Doren, "FDTD and FEM/MOM modeling of EMI resulting from a trace near a PCB edge," in Proc. *IEEE Int. Symp. Electromagn. Compat.*, Washington, D.C., Aug. 2000, pp. 135-140.

CHAPTER THREE

IMPROVEMENTS TO A METHOD FOR ESTIMATING THE MAXIMUM RADIATED EMISSIONS FROM PCBS WITH CABLES

Changyi Su and Todd Hubing

ABSTRACT

It has been shown in previous studies that the coupling from ICs, traces or heatsinks on a printed circuit board to an attached cable can be modeled by placing equivalent common-mode sources between the board and the cable. A closed-form expression has been developed to estimate the maximum radiated emissions from the board-source-cable structure [1]. While this expression is reasonably accurate for frequencies not exceeding 500 MHz, it may unnecessarily overestimate the emissions in some situations, especially when the maximum frequency of interest is extended beyond 500 MHz. This paper introduces two improvements to the closed-form expression in [1] based on improved methods to determine the maximum value of $F(\theta, k)$ and the board size. The new closed-form expression is evaluated for various board geometries and frequency ranges by comparing the estimated maximum radiated emissions to full-wave simulation results.

3.1 INTRODUCTION

Previous studies showed that the coupling from the ICs, traces or heatsinks on a printed circuit (PCB) board to an attached cable can be effectively modeled by placing equivalent voltage sources between the cable and the board [2]-[5]. The maximum radiated emissions due to the common-mode current on the cable can be estimated using

closed-form equations based on the board-equivalent-source-cable geometry [1]. The closed-form expression in [1] has been shown to be reasonably accurate for various board and cable geometries. The agreement between the estimates and the full-wave simulation results is within a few decibels at frequencies up to 500 MHz.

While this is good accuracy for a closed-form estimate, this paper presents two modifications to the original estimation method that extend the frequency range and improve accuracy of the estimate. In [1], the maximum radiated emissions were calculated using a constant, maximum value for a quantity called $F(\theta,k,l_{ant})$ associated with monopole radiation. The expression of the function is

$$F\left(\theta,k,l_{ant}\right)=\left|\frac{\cos\left(kl_{ant}\cos\theta\right)-\cos\left(kl_{ant}\right)}{\sin\theta}\right| \tag{1}$$

where θ is a variable between 0 and $\pi/2$ and l_{ant} is the monopole length above ground.

Since the envelope of $F(\theta,k,l_{ant})$ is a monotonically increasing function of frequency, this method over-estimates emission levels at low frequencies, especially at the first resonance. The over-estimation is worse when constant values of $F(\theta,k,l_{ant})$ are applied to frequency ranges extending beyond 500 MHz. Also, it was shown in [1] that maximum current is achieved when the board-source-cable geometry is approximately a quarter wavelength long. A board factor was introduced to account for the limiting effect that the board size has on the maximum field at low frequencies. The board factor is a sinusoidal function of the effective length of the board. In [1], the diagonal length of the board is used as the effective length for both rectangular and square boards. However, it

is more accurate to use an approximation that is more accurately accounts for the shape of the board.

3.2 ENVELOPE of $F(\theta, k, l_{ant})$

In [1], the closed-form expression for estimating the maximum radiation is given by,

$$|E|_{\max} = 20 \times \frac{1}{37} \times 2.76 \times board\_factor \times cable\_factor, \tag{2a}$$

where

$$board\_factor = \begin{cases} \sin\left(2\pi l_{board}/\lambda\right) & \text{when } l_{board} \le \dfrac{\lambda}{4} \\ 1.0, & \text{otherwise.} \end{cases}, \tag{2b}$$

$$cable\_factor = \begin{cases} \sin\left(2\pi l_{cable}/\lambda\right) & \text{when } l_{cable} \le \dfrac{\lambda}{4} \\ 1.0, & \text{otherwise.} \end{cases}, \tag{2c}$$

and

$$l_{board} = \sqrt{L^2 + W^2}, \tag{2d}$$

with L and W denoting the board length and width.

In this expression, the number 2.76 represents the maximum value of $F(\theta,k,l_{ant})$ in Equation (1) when the maximum frequency of interest is 500 MHz. However, the maximum value of $F(\theta,k,l_{ant})$ is not constant and increases on average with frequency. Hence, using a constant value of 2.76 tends to overestimate the values of $|E|$ at frequencies well below 500 MHz; and may underestimate the values of $|E|$ when applied to frequencies above 500 MHz.

The maximum values of $F(\theta,k,l_{ant})$ are obtained when

$$kl_{ant} = n\pi, n = 1, 2, ... \tag{3}$$

Combining Equation (3) and Equation (1), the maximum values of $F(\theta,k,l_{ant})$ are

$$\begin{aligned} F_{\max}(\theta, n) &= \left| \frac{\cos(n\pi\cos\theta) - \cos(n\pi)}{\sin\theta} \right| \\ &= \left| \frac{\cos(n\pi\cos\theta) - (-1)^n}{\sin\theta} \right| \end{aligned} . \tag{4}$$

The $cos(\theta)$ terms can be approximated by the first two terms of their Taylor's polynomials,

$$\cos\theta \approx 1 - \frac{\theta^2}{2}, \text{ when } |\theta| < \frac{\pi}{2}. \tag{5}$$

This results in a simplified version of (4),

$$F_{\max}(\theta, n) \simeq \left| \frac{1 - \cos\left(\frac{n\pi\theta^2}{2}\right)}{\sin\theta} \right|. \tag{6}$$

The maximum values of Equation (6) are achieved when $\cos\left(\frac{n\pi\theta^2}{2}\right) = -1$, or

$$\theta = \sqrt{\frac{2}{n}}. \tag{7}$$

Combining (6) and (7),

$$F_{\max}(n) \simeq \left| \frac{2}{\sin\sqrt{\frac{2}{n}}} \right|, n = 1, 2, ... \tag{8}$$

Note that θ satisfies the approximation in (5) for $n>1$. At $n=1$, the difference between (8) and (4) is 0.5 dB.

To get a continuous function that captures all the peaks, the discrete function in Equation (8) is replaced by its continuous envelope by substituting α for n,

$$F_{\max}(\alpha) \simeq \left| \frac{2}{\sin\left(\sqrt{\frac{2}{\alpha}}\right)} \right|, \tag{9}$$

where α (≥ 1) is a real continuous variable function of frequency and is given by

$$\alpha = \frac{f l_{ant}}{c_0}, \tag{10}$$

where c_0 is the velocity of light in free space.

Since $\alpha \geq 1$, the value of Equation (9) is always positive. The maximum value at $\alpha = 1$ is used for all frequencies corresponding to $\alpha < 1$.

Combing Equation (9) and (10),

$$F_{\max}(f) \simeq \begin{cases} \dfrac{2}{\sin\sqrt{2}} & f \leq \dfrac{c_0}{l_{ant}} \\ \dfrac{2}{\sin\left(\sqrt{\dfrac{c_0}{f l_{ant}}}\right)} & f > \dfrac{c_0}{l_{ant}} \end{cases}. \tag{11}$$

Figure 3.1 shows the envelope of $F(\theta,k,l_{ant})$ between 0 and 1 GHz. The green dashed line represents the maximum value of $F(\theta,kl_{ant})$ over the entire frequency range. Instead of using the maximum value, the envelope gives the exact maximum value at

each resonance. The tendency to over-estimate at the lower frequencies is eliminated and the accuracy is improved.

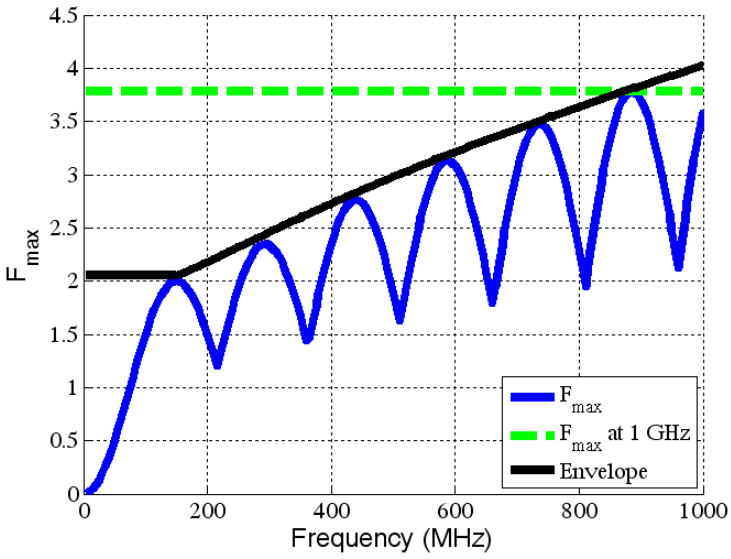

Figure 3.1. The maximum values of $F(\theta,k,l_{ant})$.

By replacing the constant 2.76 in Equation (1) with Equation (11), the new closed-form estimate for the maximum radiation can be written as

$$|E|_{\max} \simeq \begin{cases} 20\times\frac{1}{37}\times\frac{2}{\sin\left(\sqrt{2}\right)}\times board\_factor\times cable\_factor & f \le \frac{c_0}{l_{ant}} \\ 20\times\frac{1}{37}\times\frac{2}{\sin\left(\sqrt{\frac{c_0}{fl_{ant}}}\right)}\times board\_factor\times cable\_factor & f > \frac{c_0}{l_{ant}} \end{cases}. \quad (12)$$

3.3 IMPROVED EXPRESSION FOR CALCULATING THE EFFECTIVE BOARD LENGTH

In [1], the effective length of a rectangular board is approximated to be the diagonal length. This is a good approximation when the ratio of the board length to width

is large. However, a broader board tends to present a lower impedance. In other words, a nearly square board has a longer effective length than a narrow board with the same diagonal length. An empirical equation for approximating the length can be found in [7].

$$l_{eff,board} = \frac{\sqrt{L^2 + W^2}}{A}, \tag{13}$$

where A is a function of the board dimensions given by

$$A = \frac{L/2a}{1 + L/2a}, \quad a = \frac{W}{4}. \tag{14}$$

Combining (13) and (14),

$$l_{eff,board} = \frac{1 + 2L/W}{2L/W} \times \sqrt{L^2 + W^2}. \tag{15}$$

When the board is very narrow, the effective length is roughly equal to the diagonal length. As the board width increases, the effective length becomes larger than the diagonal length.

Substituting $l_{eff,board}$ (Equation 15) for l_{board} in (2b), the improved closed-form expression for the maximum radiated emission is

$$|E|_{\max} \simeq \begin{cases} 20 \times \frac{1}{37} \times \frac{2}{\sin\left(\sqrt{2}\right)} \times board\_factor \times cable\_factor & f \le \frac{c_0}{l_{ant}} \\ 20 \times \frac{1}{37} \times \frac{2}{\sin\left(\sqrt{\frac{c_0}{f l_{ant}}}\right)} \times board\_factor \times cable\_factor & f > \frac{c_0}{l_{ant}} \end{cases}, \tag{16a}$$

where

$$board\_factor = \begin{cases} \sin\left(2\pi l_{eff,board}/\lambda\right) & \text{when } l_{eff,board} \le \dfrac{\lambda}{4}, \\ 1.0, & \text{otherwise.} \end{cases} \tag{16b}$$

$$cable\_factor = \begin{cases} \sin\left(2\pi l_{cable}/\lambda\right) & \text{when } l_{cable} \le \dfrac{\lambda}{4}, \\ 1.0, & \text{otherwise.} \end{cases} \tag{16c}$$

and

$$l_{eff,board} = \frac{1+2L/W}{2L/W} \times \sqrt{L^2+W^2}\,. \tag{16d}$$

3.4 VALIDATION

To validate the new estimate, the configurations in [1] are used. Figure 3.2 shows the simplified structure of a board with attached cable, where a 1-V voltage source is connected to the center of the board. It was demonstrated in [1] that the peak emissions are relatively independent of the connection point to the board. The cable is 1 meter long and attached to an infinite ground plane.

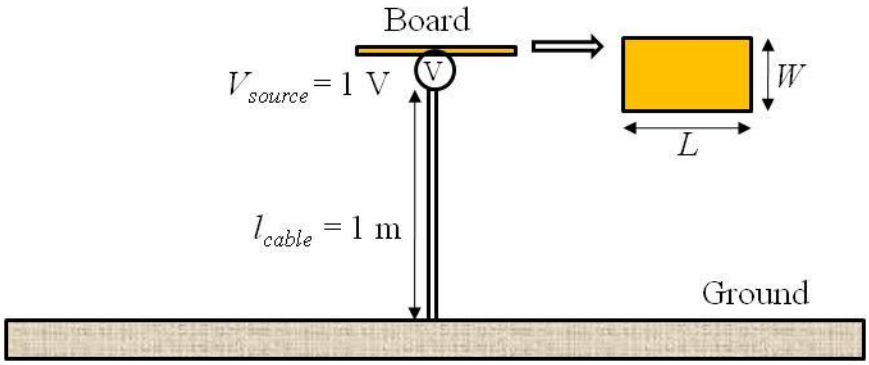

Figure 3. 2. The geometry used to validate the new estimate.

The estimates (2) and (16) are compared to full-wave simulation results [6]. Figure 3.3 shows a plot of closed-form estimates and simulation results for a 14-cm x 2-cm rectangular board. With Eq. (2), the peak emissions at low frequencies are over predicted when the maximum frequency is extended to 1GHz. The estimate using (16) eliminates the over-estimation at low frequencies and the accuracy is comparable to (2) at high frequencies. Figure 3.4 illustrates a similar plot for a 10-cm square board. The estimates are different for square and rectangular boards that have the same diagonal length. The effective length of a square board is slightly longer than that of a rectangular board and consequently the resonant frequencies of the square board are slightly shifted to the left. By using the new effective length in (15), the board factor in (16) accounts for the frequency shift at low frequencies. The maximum radiation for a 63-cm x 9-cm rectangular board and a 45-cm square board are plotted in Figure 3.5 and Figure 3.6, respectively. The closed-form expression in (16) does a reasonable job of estimating the maximum emissions for large board dimensions.

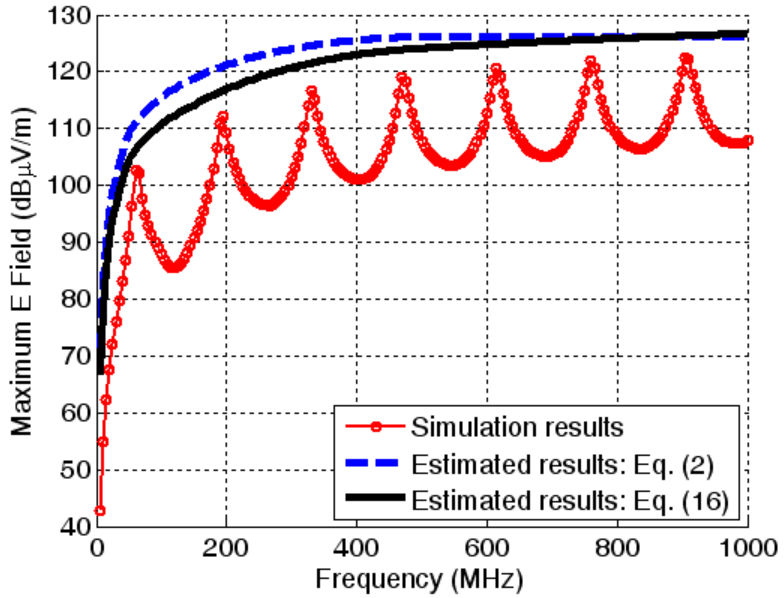

Figure 3.3. Maximum radiation for a 14-cm x 2-cm rectangular board (1-m cable).

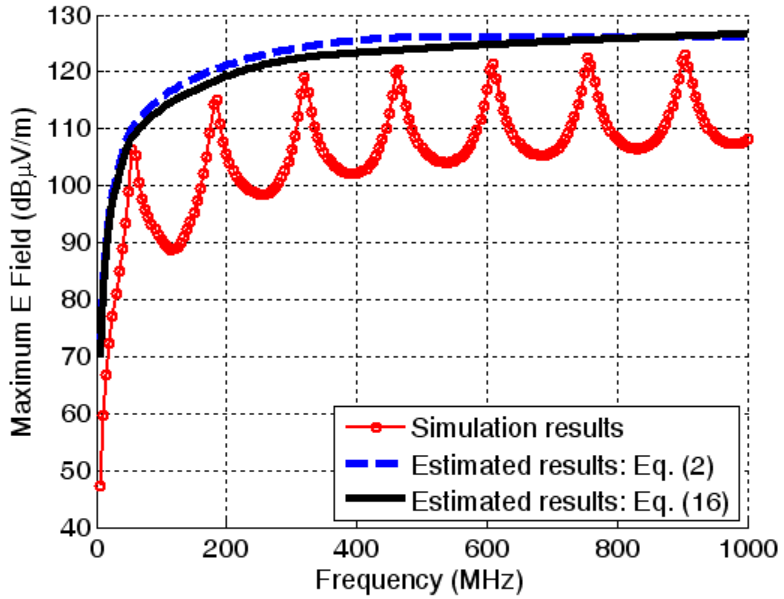

Figure 3.4. Maximum radiation for a 10-cm square board (1-m cable).

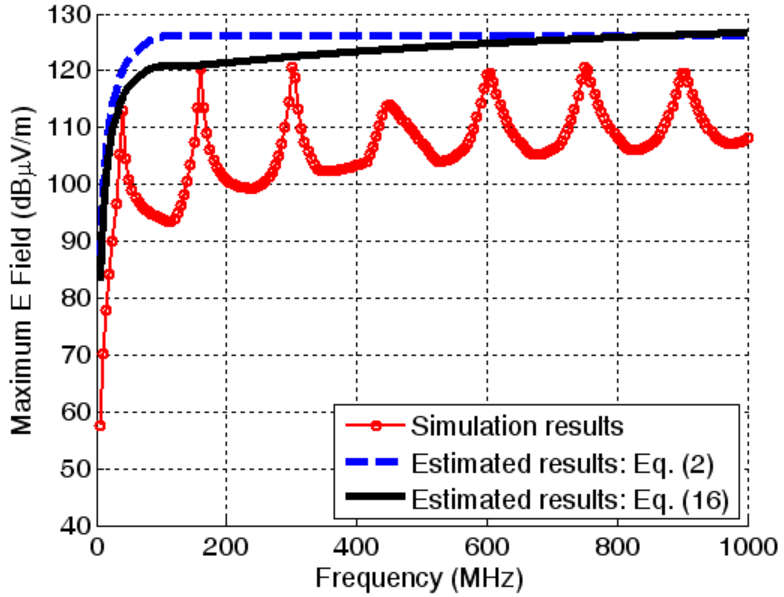

Figure 3.5. Maximum radiation for a 63-cm x 9-cm rectangular board (1-m cable).

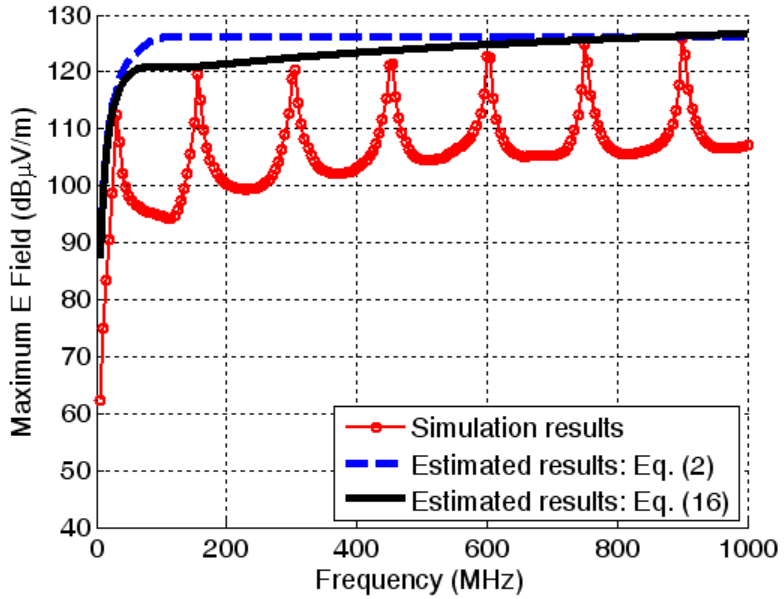

Figure 3.6. Maximum radiation for a 45-cm square board (1-m cable).

The improvement in the accuracy of the estimate is even greater when the maximum frequency is further extended. To illustrate this, the configuration in Figure 3.6 was evaluated between 10 MHz and 3 GHz, as shown in Figure 3.7. Since the value 2.76 in (2) only applies to frequencies up to 500 MHz, this constant as replaced by another constant, 6.78, which is the maximum value of $F(\theta,k,l_{ant})$ for frequencies up to 3 GHz. Note that this causes the lower frequency peaks to be significantly over-estimated. The closed-form expression in (16) improves the estimation by using the exact maximum values of $F(\theta,k,l_{ant})$ at every resonant frequency. The accuracy at low frequencies is improved by up to 10 dB.

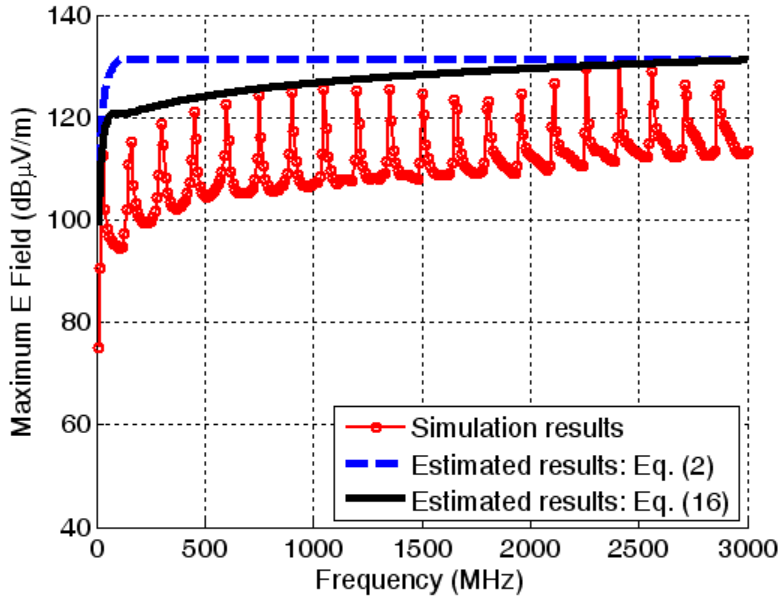

Figure 3.7. Maximum radiation for a 45-cm square board up to 3 GHz.

3.5 CONCLUSIONS

This paper describes two improvements to the method introduced in [1]. The accuracy of the estimate for larger frequency ranges is improved by using an expression for the envelope of $F(\theta, kl_{ant})$ that equals the maximum value at every resonant frequency. A modified expression for calculating the effective length of the board improves the accuracy of the estimate when applied to nearly square boards.

REFERENCES

[1] S. Deng, T. Hubing and D. Beetner, "Estimating maximum radiated emissions from printed circuit boards with an attached cable," *IEEE Trans. Electromagn. Compat*., vol. 50, no. 1, pp. 215-218, Feb. 2008.

[2] D. M. Hockanson, J. L. Drewniak, T. H. Hubing, T. P. Van Doren, F. Sha, and M. Wilhelm, "Investigation of fundamental EMI source mechanisms driving common-mode radiation from printed circuit boards with attached cables," *IEEE Trans. Electromagn. Compat*., vol. EMC-38, no. 4, pp. 557-566, Nov. 1996.

[3] W. Cui, H. Shi, X. Luo, J. L. Drewniak, T. P. Van Doren, and T. Anderson, "Lumped-element sections for modeling coupling between high-speed digital and I/O lines," in *Proc. IEEE Int. Symp. Electromagn. Compat.*, Austin, Texas, Aug., 1997, pp. 260-265.

[4] N. Oka, C. Miyazaki, and S. Nitta, "Radiation from a PCB with coupling between a low frequency and a digital signal traces," in *Proc. IEEE Int. Symp. Electromagn. Compat.*, Aug 1998, pp. 635 – 640.

[5] H. Shim and T. Hubing, "Model for estimating radiated emissions from a printed circuit Board with attached cables driven by voltage-driven sources," *IEEE Trans. Electromagn. Compat.*, vol. 47, no. 4, pp. 899-907, Nov. 2005.

[6] FEKO User's Manual, Suite 6.0, September, 2010.

[7] J. D. Kraus, *Antennas*, McGraw-Hill, New York, 1950, pp. 276-278.

CHAPTER FOUR

CALCULATING RADIATED EMISSIONS DUE TO I/O LINE COUPLING ON PRINTED CIRCUIT BOARDS USING THE IMBALANCE DIFFERENCE METHOD

Changyi Su and Todd Hubing

ABSTRACT

High frequency signals on printed circuit board traces can couple to input/output (I/O) nets that carry the coupled energy away from the board and result in significant radiated emissions. A modeling technique is proposed to speed up the analysis of printed circuit boards (PCBs) with coupled microstrip lines that induce common-mode currents on attached cables. Based on the concept of imbalance difference, differential-mode sources are converted to equivalent common-mode sources that drive the attached cable and the PCB reference plane. A closed-form expression based on the imbalance difference model is developed to estimate the maximum radiated emissions due to I/O line coupling in PCBs.

4.1 INTRODUCTION

Crosstalk is a major concern for PCB designers. Coupling between signal lines can cause electromagnetic interference (EMI) issues as well as signal integrity (SI) problems. Crosstalk between signal traces and traces that connect to wires that bring signals or power onto the board (I/O lines) can be particularly troublesome. Although crosstalk can be minimized by careful rooting of signal and I/O traces, there are times

when a designer has no alternative but to allow some amount of crosstalk in their design. Calculating levels of crosstalk is particularly challenging when one of traces is an I/O trace, because the termination impedance of the trace may be unknown.

One approach for analyzing the radiated emissions due to coupling between signal and I/O lines in a PCB is through simulation of the interconnect system using a 3D full-wave electromagnetic modeling (EM) simulator. Full-wave models can provide accurate solutions to well-defined problems, but they require significant computational resources and they cannot predict how small changes in the structure will affect the results without repeating the analysis with these changes made. Full-wave models are not practical option for providing fast estimates of worst-case radiated emissions during the initial design and routing processes. An alternative approach is to divide the entire I/O coupling problem into three essential components:

1) Calculating the voltages coupled to the I/O line circuit;

2) Modeling the wire/board structure as an antenna;

3) Determining the maximum radiated emissions from this source/antenna structure.

Extensive research has been devoted to developing fast and accurate techniques for crosstalk analysis [1]-[4], the first component of this problem. Less research has been done on the antenna model and the radiated emission estimation, but simple equations were derived by assuming the attached cable was an isotropic radiator in [5]. A maximum radiated field estimate based on a dipole antenna model was presented in [6]-[9]. In this model, a common-mode voltage source was applied between the cable and the PCB

reference plane at the connector; but the input impedance of the antenna was required to determine the magnitude of the common-mode voltage. In the previous papers, either simulations [7] or measurements [8] were used to obtain the impedance of the antenna. In [9], a worst-case estimate of the antenna impedance, based on a resonant half-wave dipole, was used. This method did not require simulation or measurement of the input impedance of the antenna and provided a reasonable estimate of the worst-case radiated emissions. However, it did not calculate the field strength at frequencies between the resonances. Finally, the effects of eliminating the coupled lines and the dielectric layer from the antenna model were also unclear. An equivalent model which includes the I/O line and part of the dielectric layer was proposed in [10]. However, these details significantly increased the simulation time.

In Section 4.2, the Thevenin equivalent source coupled to the I/O circuit is determined. Section 4.3 introduces a model for calculating the radiated emissions due to I/O coupling on PCBs that significantly reduces simulation times without sacrificing the accuracy of the results. The model is derived based on the concept of imbalance difference [11]-[15]. The differential-mode signals on the signal traces are converted to equivalent common-mode sources quantitatively using a parameter called the imbalance factor. In the imbalance difference model, the lines carrying differential signals on the PCB are replaced by equivalent common-mode sources. This model separates the radiation problem from the PCB coupling problem and provides a fast way to estimate the radiated fields from the PCB due to coupling between signal and I/O lines. In Section 4.4, a closed-form expression is developed based on the imbalance difference model to

predict the maximum radiation from the PCB. The accuracy of the model and the closed-form expression are evaluated for various test geometries in Section 4.5.

4.2 THEVENIN EQUIVALENT COUPLING SOURCE

A schematic illustrating the coupling from a high-speed signal trace to an adjacent I/O line is shown in Figure 4.1. The signal trace and the I/O line are routed next to each other over a wide ground plane. The traces are on the same layer without conducting planes between them. The signal trace is connected to a signal source at one end and terminated with a load at the other end. The I/O trace is terminated with a resistance at the near-end and a wire extending beyond the return plane at the far-end. The signal can be coupled to the I/O circuit by two coupling mechanisms: magnetic-field coupling or electric-field coupling. Magnetic-field (or inductive) coupling occurs when the magnetic field lines from the source circuit, pass through the loop formed by the I/O trace circuit and return plane. Schematically, magnetic coupling is represented by a mutual inductance (L_m) between the two loops. Similarly, a mutual capacitance (C_m) between the two traces is used to indicate that energy is coupled from the source circuit to the victim circuit through an electric field (i.e. capacitive coupling).

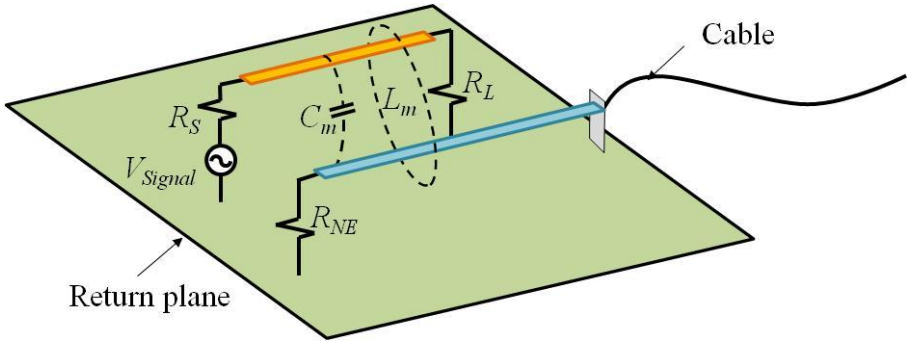

Figure 4.1. Schematic representation of signal coupling to an I/O line.

In this paper, the analysis of this problem will be broken into three distinct stages:

1) Developing the equivalent lumped-element circuit model for the two coupling mechanisms and determining the total voltage coupled to the victim circuit;
2) Developing a relative simple imbalance difference model for the complex geometry;
3) Analyzing the simplified model to determine either the actual or worst-case radiated emissions.

To calculate the crosstalk between the coupled lines, consider the equivalent circuit shown in Figure 4.2. A source circuit consists of a source voltage (V_{signal}) and a source impedance (Z_S) which is connected to a load (Z_L) via a signal trace. Two other terminations, denoted as Z_{NE} and Z_{FE}, are connected to an I/O trace. The circuit terminations are known and have variable values, with the exception of the far-end load of the I/O trace (Z_{FE}), where the cable is attached. The equivalent impedance looking into the attached cable is actually the input impedance of an antenna which is driven by the induced voltage at the connector.

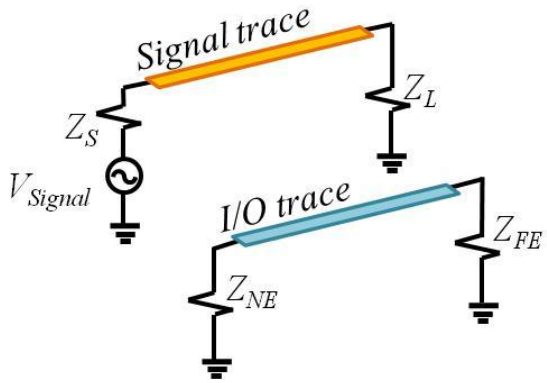

Figure 4.2. Equivalent circuit illustrating crosstalk.

Two types of coupling induce noise in the victim circuit, i.e. the inductive coupling and the capacitive coupling. By assuming the lines are weakly coupled, the total coupling is a linear combination of contributions due to these two coupling mechanisms [3]. In Figure 4.3, the I/O trace and return plane is represented as a transmission line of length *l*. One end of the transmission line is connected to a voltage source (V_{ind}) which represents the induced *EMF* due to inductive coupling.

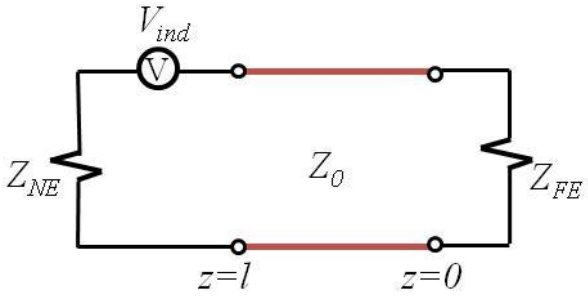

Figure 4.3. The magnetic coupling model of the victim circuit.

By assuming the signal trace is electrically short, the induced voltage due to inductive coupling is given by

$$\hat{V}_{ind} = -j\omega L_m \frac{1}{Z_S + Z_L} \hat{V}_{Signal} \tag{1}$$

where L_m is the mutual inductance between the signal trace circuit and the I/O trace circuit.

In Figure 4.4, an independent current source (I_{cap}) represents the induced current due to capacitive coupling.

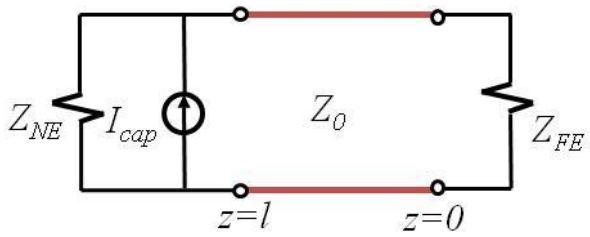

Figure 4. 4. The capacitive coupling model of the victim circuit.

The induced current source amplitude is

$$\hat{I}_{cap} = j\omega C_m \frac{Z_L}{Z_S + Z_L} \hat{V}_{Signal} \tag{2}$$

where C_m is the mutual capacitance between the signal trace circuit and the I/O trace circuit.

The total voltage induced in the victim circuit is the linear superposition of the two equivalent coupling sources,

$$\hat{V}_{total} = \hat{V}_{ind} + \hat{V}_{cap}$$
$$= j\omega\left[-L_m \frac{1}{Z_S + Z_L} + C_m \frac{Z_{NE} Z_L}{Z_S + Z_L}\right]\hat{V}_{Signal} \quad . \tag{3}$$

At low frequencies, the I/O trace can be approximated as lossless transmission line and the voltage at the connector is readily calculated from transmission line theory [16]. As shown in Figure 4.5(a), the I/O line structure in Figure 4.1 is represented as a transmission line of length *l* connected on one end to a source circuit and on the other end to a load (Z_{FE}). The circuit in Figure 4.5(b) is the Thevenin equivalent of the circuit in Figure 4.5(a).

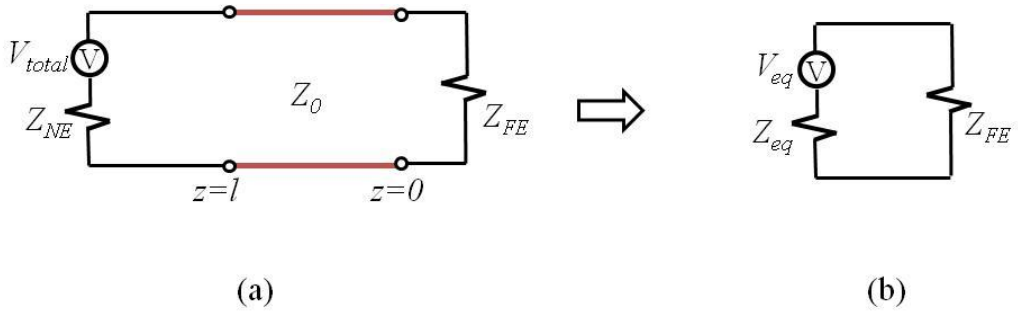

Figure 4.5. Equivalent circuits for the I/O line structure, (a) transmission line circuit, (b) Thevenin equivalent circuit.

The Thevenin equivalent source driving Z_{FE} consists of an equivalent voltage source (V_{eq}) and equivalent impedance (Z_{eq}). The general solution for voltage on a lossless transmission line is

$$\hat{V}(z) = V_0^+ e^{-j\beta z} + V_0^- e^{j\beta z}, \tag{4}$$

where V_0^+ and V_0^- are the voltage amplitudes of the incident and reflected waves, respectively. The Thevenin voltage for the circuit in Figure 4.5(a) is

$$\hat{V}_{eq} = \hat{V}_{total}\left(z=0\right) = V_0^+ + V_0^- = V_0^+\left(1+\Gamma\right). \tag{5}$$

When calculating the open-circuit voltage, the reflection coefficient is one since the load side is open. Therefore, Equation (5) becomes

$$\hat{V}_{eq} = V_0^+ + V_0^- = 2V_0^+. \tag{6}$$

where V_0^+ is given by

$$V_0^+ = \left(\frac{\hat{V}_{total} Z_{in}}{Z_{in} + Z_{NE}}\right)\left(\frac{1}{e^{j\beta l} + e^{-j\beta l}}\right). \tag{7}$$

Z_{in} is the input impedance looking toward the open-circuit load and is given by

$$Z_{in} = \frac{Z_0}{j\tan\beta l}, \tag{8}$$

where Z_0 is the characteristic impedance of the transmission line and β is the wave number.

Combining Equations (6) and (7), leads to the result

$$\hat{V}_{eq} = 2\left(\frac{Z_0}{Z_0 + jZ_{NE}\tan\beta l}\right)\left(\frac{\hat{V}_{total}}{e^{j\beta l} + e^{-j\beta l}}\right). \tag{9}$$

Replacing V_{total} with Equation (3), the magnitude of $\hat{V}_{eq}$ is

$$\left|\hat{V}_{eq}\right| = \left|\frac{\hat{V}_{Signal}}{\cos\beta l}\right|\left|\frac{Z_0}{Z_0 + jZ_{NE}\tan\beta l}\right|\left|-\omega L_m \frac{1}{Z_S + Z_L} + \omega C_m \frac{Z_{NE} Z_L}{Z_S + Z_L}\right|. \tag{10}$$

The Thevenin equivalent impedance is

$$Z_{eq} = Z_0 \left(\frac{Z_{NE} + jZ_0 \tan \beta l}{Z_0 + jZ_{NE} \tan \beta l} \right). \tag{11}$$

The mutual inductance and capacitance in Equation (10) can be calculated based on the concept of even-mode and odd-mode capacitances of coupled microstrip lines on a printed circuit board [17].

4.3 THE IMBALANCE DIFFERENCE MODEL

In section 4.2, the complex geometry in Figure 4.1 was simplified by removing the signal trace circuit and applying the total induced voltage source to the victim circuit, as shown in Figure 4.6(a). The development of the simplified circuit in Figure 4.6(a) does not require any prior knowledge of the impedance at the cable end of the I/O circuit. In this section, the structure in Figure 4.6(a) is further simplified using the imbalance difference theory first proposed by Watanabe [11] and further developed in [12]-[15]. According to this theory, the common-mode current on the cable in Figure 4.6(a) is equivalent to the current on the cable in Figure 4.6(b). In Figure 4.6(b), the ground plane is driven against the cable by two common-mode sources. The amplitude of each common-mode source is the product of the differential-mode voltage and the change in the imbalance factor that occurs at teach end of the I/O trace. Since the width of the trace is much smaller than that of the board, the change in the imbalance at the source end of the trace is very close to zero. Hence, the magnitude of the first common-mode source (V_{CM1}) is close to zero. The change in the imbalance factor at the other end is very close to 1. Therefore, the magnitude of the second common-mode source (V_{CM2}) is

approximately equal to the differential-mode voltage (V_{FE}) at the connector. With thee approximations, the equivalent model in Figure 4.6(b) can be further simplified to Figure 4.6(c) in which the board is driven by the differential-mode voltage at the load end of the I/O trace.

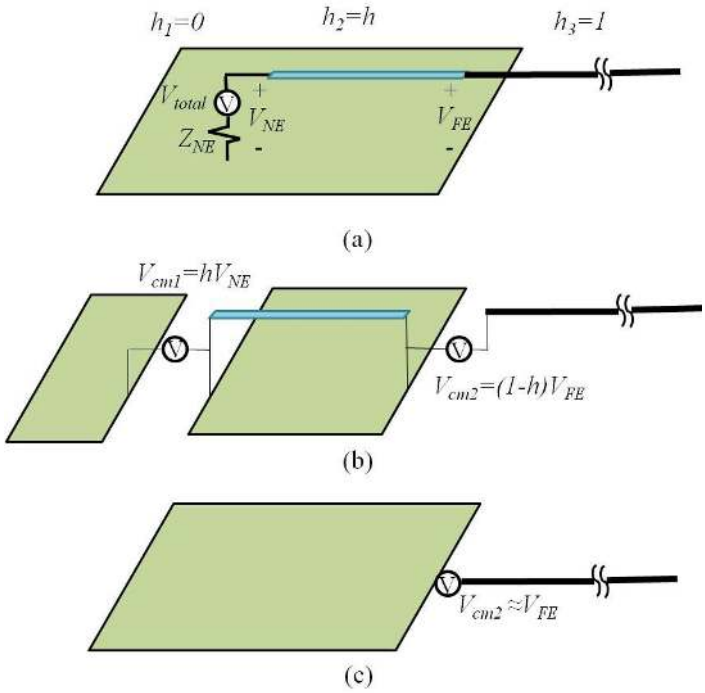

Figure 4.6.The imbalance difference model for the I/O line structure, (a) full model (b) imbalance difference model (c) simplified imbalance difference model.

From the circuit in Figure 4.6(c), the voltage driving the cable depends on the value of the antenna impedance. The input impedance of the dipole-type antenna in Figure 4.6(c) is a complex function of frequency that can only be determined by full-wave simulation or measurement. To avoid doing this, the equivalent model in Figure 4.6(c) is replaced by the model in Figure 4.7. In the new model, the Thevenin equivalent

source in Figure 4.5(b) is substituted for the common-mode source in Figure 4.6(c). For cable current calculations, the simplified source in Figure 4.7 is equivalent to the original circuit in Figure 4.1 and does not require any assumptions about the antenna input impedance.

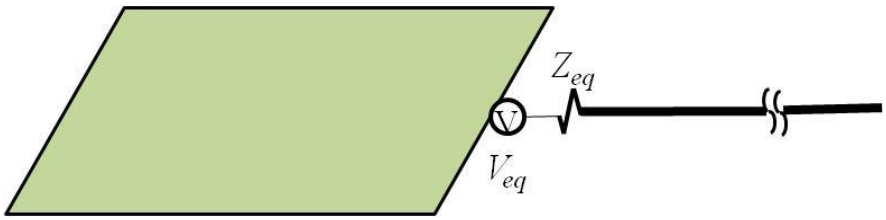

Figure 4.7. Imbalance difference model.

In Figure 4.7, both the I/O line and the dielectric layer were deleted from the model. While these play an important role in full-wave simulations of the entire structure, they are relatively unimportant after the amplitude of the common-mode source is determined. To achieve the highest degree of accuracy, they can be left in the model, but eliminating the I/O line and the dielectric layer from the equivalent model significantly reduces the simulation time while still yielding good results.

4.4 MAXIMUM RADIATED EMISSION ESTIMATION

A full-wave analysis of the radiated emissions from the simplified model in Figure 4.7 will yield virtually the same results as a full-wave analysis of the much more complex configuration in Figure 4.1. However, very often for EMC problem analysis, it is much more useful to obtain the maximum emissions from the PCB with all possible cable lengths and orientations than it is to obtain the emission from one specific cable

geometry. A closed-form formula was developed in [18] to estimate the maximum radiated electric field from the antenna model in Figure 4.7. This formula was enhanced in [19] to be more accurate over larger frequency ranges. When a board is driven by an ideal common-mode source, V_{CM}, the maximum electric field can be calculated as

$$|E|_{\max} \simeq \begin{cases} 20 \times I_{peak} \times \dfrac{2}{\sin\left(\sqrt{2}\right)} & f \le \dfrac{c_0}{l_{cable}} \\ 20 \times I_{peak} \times \dfrac{2}{\sin\left(\sqrt{\dfrac{c_0}{f l_{cable}}}\right)} & f > \dfrac{c_0}{l_{cable}} \end{cases}, \tag{12}$$

where l_{cable} is the length of the attached cable, f is the frequency, and c_0 is the propagation velocity in free space. I_{peak} is the highest current that actually exists on the cable and is given by

$$I_{peak} = \frac{V_{CM}}{\dfrac{R_{\min}}{board\_factor \times cable\_factor}}. \tag{13}$$

R_{min} is the input resistance of a resonant quarter-wave monopole. Two factors were defined to account for the effect that the finite cable length and the small board size have on this minimum resistance

$$board\_factor = \begin{cases} \sin\left(2\pi l_{board}/\lambda\right) & \text{when } l_{board} \le \dfrac{\lambda}{4} \\ 1.0, & \text{otherwise.} \end{cases}, \tag{14}$$

$$cable\_factor = \begin{cases} \sin\left(2\pi l_{cable}/\lambda\right) & \text{when } l_{cable} \le \dfrac{\lambda}{4} \\ 1.0, & \text{otherwise.} \end{cases}, \tag{15}$$

and

$$l_{board} = \frac{1 + 2L/W}{2L/W} \times \sqrt{L^2 + W^2},$$

where L and W denote the board length and width.

The common-mode source in Figure 7 is connected to the equivalent impedance, Z_{eq}. Since this impedance value is not affected by the cable length and source location, the highest current on the cable can be written as

$$I_{peak} = \frac{V_{eq}}{\left| Z_{eq} + \frac{R_{\min}}{board\_factor \times cable\_factor} \right|}. \quad (16)$$

For the model in Figure 7, Equations (12) - (16) can be used to estimate the maximum radiated electric field strength at a distance of 3 meter from the board.

4.5 VALIDATION

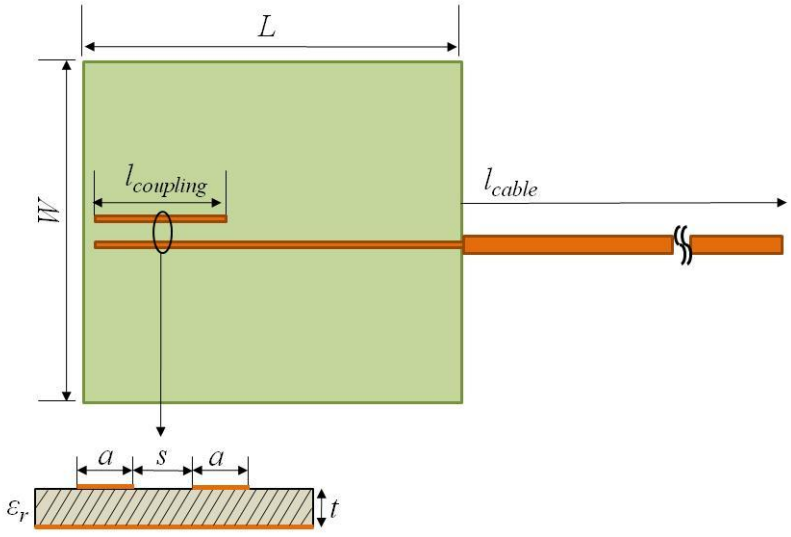

Figure 4.8. Test geometry.

In order to validate the equivalent model in Figure 4.7, the radiated fields from various I/O coupling geometries were calculated using a full-wave numerical modeling code [20]. The modeled test board and the coupled traces are shown in Figure 4.8. The test board has a dimensions *L* x *W*. The traces have a microstrip line structure. A cross-sectioned view of the coupled microstrip line structure is also shown in Figure 4.8.The signal trace is driven by a 1-V, 50-Ω voltage source at one end and terminated with a 50-Ω load at the other end. An I/O trace is routed parallel with the signal trace and extended beyond the board as 1 meter long cable with negligible diameter. The near-end of the I/O trace is terminated with a 50-Ω resistor. The space between the traces and the ground plane is filled with a dielectric material with a dielectric constant, ε_r.

To validate the imbalance difference model and the closed-form expression in Equations (12) - (16), both the geometry and the dielectric constant were varied as listed in Table 4.1. The geometrical parameters include the trace width-to-height ratio (*a/t*), the separation-to-height ratio (*s/t*), the coupling length, and the board width.

Table 4.1. Simulation configurations.

No	Geometrical parameters					Dielectric constant ε_r
	a/h	*s/h*	$L_{coupling}$ (mm)	*L (mm)*	*W (mm)*	
1	0.5	0.5	20	100	100	1.0
2	0.5	1.0	20	100	100	1.0
3	1.0	0.5	20	100	100	1.0
4	0.5	0.5	40	100	100	1.0
5	0.5	0.5	20	100	40	1.0
6	0.5	0.5	20	100	100	4.0

Figure 4.9 shows a plot of the simulation results from the model of the entire configuration and the corresponding imbalance difference model, together with the maximum emissions estimate for Case 1. The imbalance difference model yields results that are in good agreement with the original configuration over the entire 10-1000 MHz frequency range. The closed-form expression estimates the peak emissions from the board within a few decibels at every resonant frequency. Figures 4.10-4.13 show similar plots for test cases 2-5. In all cases, the difference between the simulation and the estimate is within a few decibels.

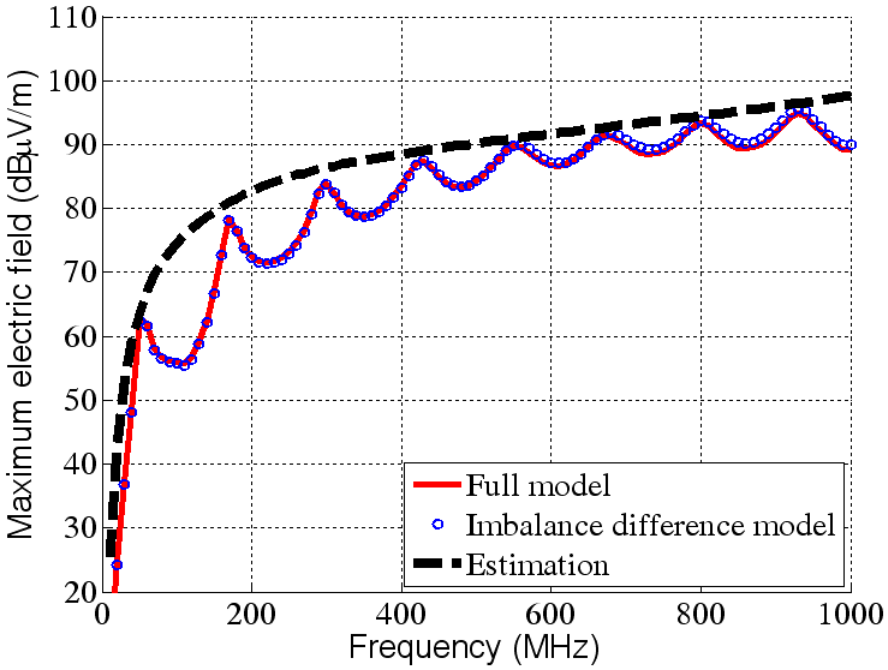

Figure 4.9. Maximum radiation for Case 1.

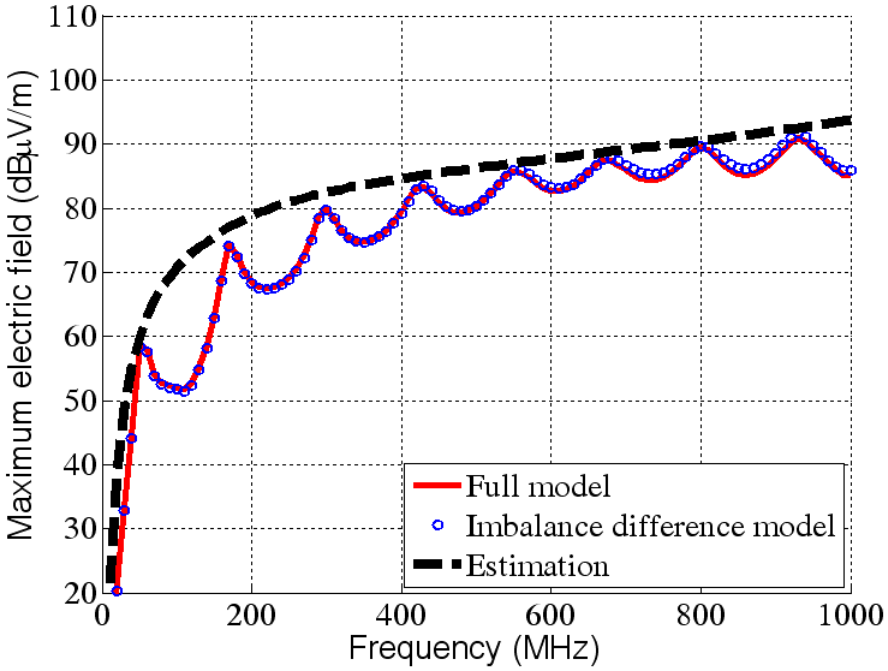

Figure 4.10. Maximum radiation for Case 2.

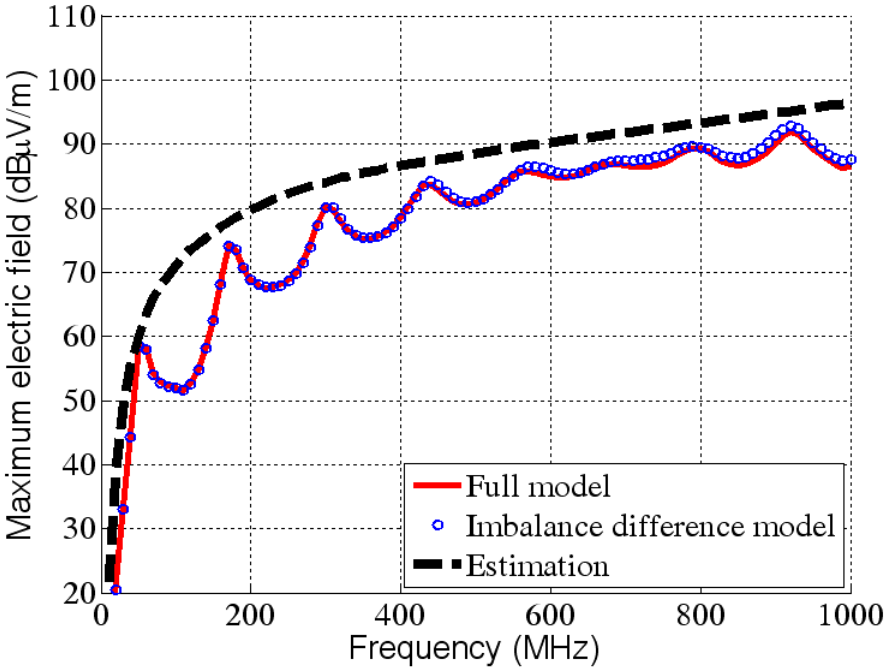

Figure 4.11. Maximum radiation for Case 3.

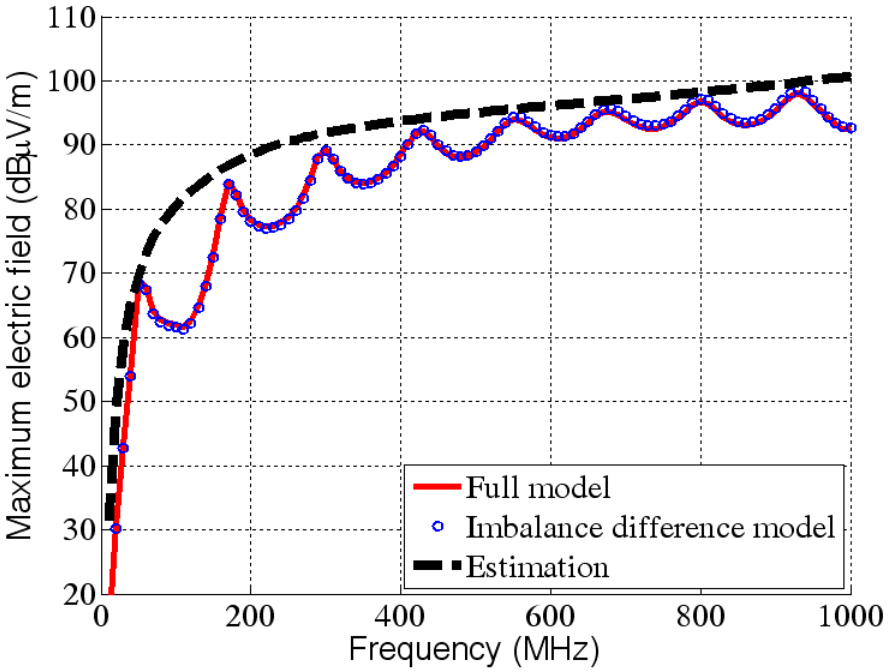

Figure 4.12. Maximum radiation for Case 4.

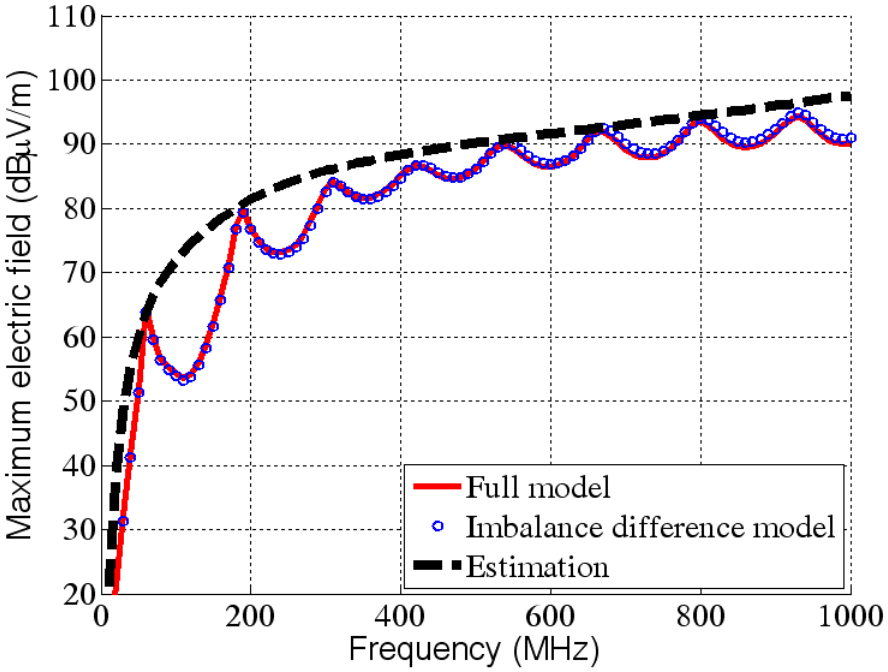

Figure 4.13. Maximum radiation for Case 5.

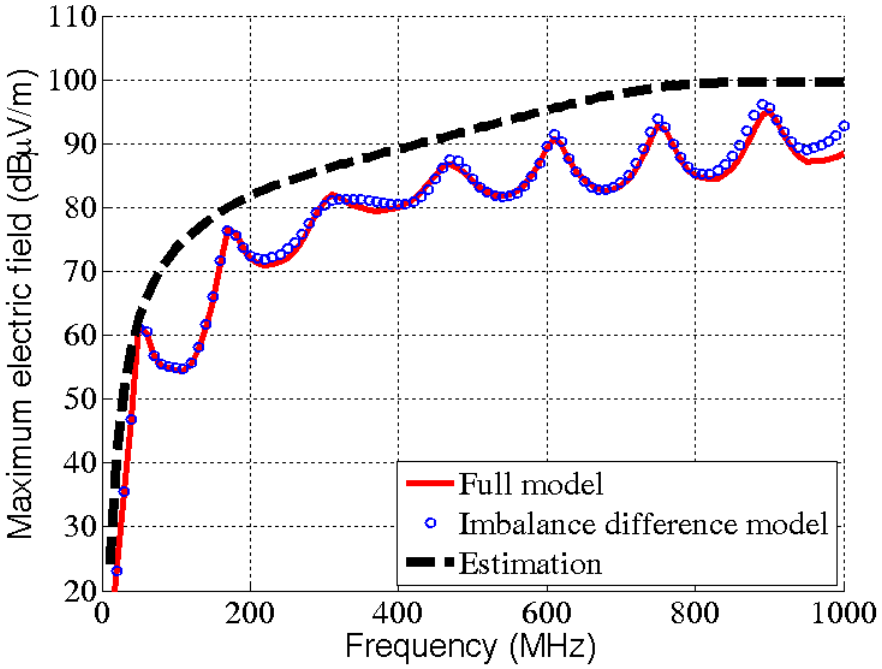

Figure 4.14. Maximum radiation for Case 6.

In Case 6, where the dielectric constant is 4.0, the agreement between the full model (with dielectric) and the imbalance difference model (no dielectric) is excellent. This demonstrates that the presence of the dielectric is no longer required after the model has been simplified using the imbalance difference model. Eliminating the dielectric layer from the imbalance difference model significantly reduces the simulation time without sacrificing the accuracy of the results.

4.6 CONCLUSIONS

An equivalent source/imbalance difference model for printed circuit boards with coupling between high-speed traces and I/O traces has been presented. In this model, the

differential-mode sources and traces are replaced with a common-mode voltage source that drives the attached cable against the reference plane. The fine structures of the traces are eliminated in the equivalent model; and therefore, analysis of the equivalent model requires much less computational resources than an analysis of the full model. Based on the imbalance difference model, a closed-form expression was also presented that estimates the maximum radiated emissions from the PCB-cable structure.

REFERENCES

[1] B. D. Jarvis, "The effects of interconnections on high-speed logic circuits," *IEEE Trans. Electron. Comput*., vol. 12, pp. 476–487, Oct. 1963.

[2] J. A. DeFalco, "Predicting crosstalk in digital systems," *Comput. Design*, vol. 12, no. 6, pp. 69–75, June 1973.

[3] C. Paul, *Introduction to Electromagnetic Compatibility*, New York: John Wiley & Sons, Inc., 1992.

[4] C. R. Paul, *Analysis of Multiconductor Transmission Lines*, New York, NY: John Wiley & Sons, Inc., 1994.

[5] H. Shim, T. Hubing, T. Van Doren, R. DuBroff, J. Drewniak, D. Pommerenke, and R. Kaires, "Expert system algorithms for identifying radiated emission problems in printed circuit boards," in *Proc. IEEE Int. Symp. Electromagn. Compat.*, Santa Clara, CA, vol. 1, Aug. 9–13, 2004, pp. 57–62.

[6] N. Oka, C. Miyazaki, and S. Nitta, "Radiation from a PCB with coupling between a low frequency and a digital signal traces," in *Proc. IEEE Int. Symp. Electromagn. Compat*., Aug 1998, pp. 635 – 640.

[7] W. Cui, M. Li, J. Drewniak, T. Hubing, T. Van Doren, R. DuBroff and X. Luo, "Anticipating EMI from coupling between high-speed digital and I/O lines," in *Proc. IEEE Int. Symp. Electromagn. Compat*., Seattle, WA, Aug. 1999, pp. 189-194.

[8] M. Tanaka, W. Cui, X. Luo, J. L. Drewniak, T. H. Hubing, T. P. Van Doren, R. E. DuBroff, "FDTD modeling of EMI antennas," in *Proc. IEEE Int. Symp. Electromagn. Compat*., 1999, pp.560-563.

[9] W. Cui, H. Shi, X. Luo, J. L. Drewniak, T. P. Van Doren, and T. Anderson, "Lumped-element sections for modeling coupling between high-speed digital and I/O lines," in *Proc. IEEE Int. Symp. Electromagn. Compat*., Austin, Texas, Aug., 1997, pp. 260-265.

[10] S. Ohtsu, K. Nahase, and T. Yamagajou, "Analysis of radiation caused by LSI package cross talk and cable by using the time-domain moment method," in *Proc. IEEE Int. Electromagn. Compat. Symp*., Aug. 2002, pp. 268–272.

[11] T. Watanabe, O. Wada, T. Miyashita and R. Koga, "Common-mode-current generation caused by difference of unbalance of transmission lines on a printed circuit board with narrow ground pattern," *IEICE Transactions on Communications*, vol. E83-B, no. 3, March 2000, pp. 593-599

[12] T. Watanabe, S. Matsunaga, O. Wada, M. Kishimoto, T. Tanimoto, A. Namba, and R. Koga, "Equivalence of two calculation methods for common-mode excitation on a printed circuit board with narrow ground plane," in *Proc. IEEE Symp. Electromagn. Compat*., Boston, MA, Aug. 2003, pp. 22–27.

[13] Y. Toyota, T. Matsushima, K. Iokibe, R. Koga, T. Watanabe, "Experimental validation of imbalance difference model to estimate common-mode excitation in PCBs," in *Proc. IEEE Symp. Electromagn. Compat.*, Detroit, Aug. 2008, pp. 1-6.

[14] T. Matsushima, T. Watanabe, Y. Toyota, R. Koga, and O. Wada, "Prediction of EMI from two-channel differential signaling system based on imbalance difference model," in *Proc. IEEE Symp. Electromagn. Compat.*, Fort Lauderdale, Jul. 2010, pp. 413-418.

[15] C. Su and T. Hubing, "Imbalance Difference Model for Common-mode Radiation from Printed Circuit Boards," *IEEE Trans. Electromagn. Compat*., vol. 53, no. 1, Feb. 2011.

[16] D. M. Pozar, *Microwave Engineering*, New York, John Wiley & Sons Inc, 2005.

[17] K. C. Gupta, Ramesh Garg, Inder Bahl, and Prakash Bhartia, *Microstrip Lines and Slotlines*, 2nd edition, Artech House, Norwood, MA, 1996.

[18] S. Deng, T. Hubing and D. Beetner, "Estimating maximum radiated emissions from printed circuit boards with an attached cable," *IEEE Trans. Electromagn. Compat*., vol. 50, no. 1, pp. 215-218, Feb. 2008.

[19] C. Su, and T. Hubing, "Improvements to a method for estimating the maximum radiated emissions from PCBs with cables," CVEL technical report, CVEL-11-024, March, 2011.

[20] FEKO User's Manual, Suite 6.0, September, 2010.